Title
Rational design of platinum-based ultrafine nanowire material for superior electro-catalytic properties

Author
Li, Mufan

Publication Date
2017

Peer reviewed|Thesis/dissertation

UNIVERSITY OF CALIFORNIA

Los Angeles

Rational design of platinum-based ultrafine nanowire material for superior electro-catalytic properties

A dissertation submitted in partial satisfaction of the

requirements for the degree Doctor of Philosophy

in Chemistry

by

Mufan Li

2017

ABSTRACT OF THE DISSERTATION

Rational design of platinum-based one dimensional nanomaterial

for superior electro-catalytic properties

by

Mufan Li

Doctor of Philosophy in Chemistry

University of California, Los Angeles, 2017

Professor Xiangfeng Duan, Chair

Oxygen reduction reaction (ORR) and hydrogen evolution (HER) are two critical electro-chemical reactions for proton exchange membrane fuel cell (PEMFC) applications. However, both ORR and HER need catalysts to overcome their respective kinetic barrier, and noble metal platinum has been proved to be the most active element to catalyze both reactions. Due to the extreme sacristy and high price of Pt, promoting the Pt mass activity (activity per given Pt mass) present the key challenge for electro-catalyst design. Improving the Pt mass activity should optimize both the specific activity and the electrochemical active surface area (ECSA) simultaneously. In first part of my dissertation, we show that solution-synthesized Pt/NiO core/shell nanowires can be readily converted into PtNi alloy nanowires through a post-synthesis

thermal annealing process, and then transformed into jagged Pt nanowires (J-PtNWs) via an electrochemical dealloying. The jagged nanowires exhibit an ECSA of 118 meter square per gram Pt and a specific activity of 11.5 milliamperes per square centimeter for ORR (at 0.9 Volt versus the reversible hydrogen electrode) for a mass activity of 13.6 ampere per milligram Pt, or nearly doubles previously reported best values. Reactive molecular dynamics simulations suggest that highly stressed, undercoordinated rhombahedral-rich surface configurations of the jagged nanowires enhanced ORR activity versus more relaxed surfaces. In second part of my dissertation, we developed a controlled electro-chemical approach to modify jagged platinum nanowire with nickel hydroxide species [J-PtNWs/$Ni(OH)_2$]. The result materials feature rich surface defects and locally decorated $Ni(OH)_2$ species as bifunctional catalysts for highly efficient electro-catalytic water splitting. Electrocatalytic studies show that J-PtNWs/$Ni(OH)_2$ exhibits extraordinary activity for hydrogen evolution reactions (HER) with a record high mass activity of 11.8 A/mg_{Pt} at -70 mV versus reversible hydrogen electrode (RHE) at pH 14, which is 17 times higher than that of Pt/C catalyst and 9 times higher than best HER performance reported to date. Density functional theory calculations demonstrate that defective surface offers an ensemble of highly active sites, and that surface $Ni(OH)_2$ species further tune the hydrogen binding energy towards optimal value. Moreover, we further show such surface modification could also greatly enhance the catalytic activity towards the oxygen evolution reaction (OER) and enable a bifunctional catalyst for highly efficient water splitting with a mass activity of 0.6 A/mg_{Pt} at 1.6 V vs. RHE.

The dissertation of Mufan Li is approved.

Alexander Michael Spokoyny

Yu Huang

Xiangfeng Duan, Committee Chair

University of California, Los Angeles

2017

Dedicated to my farther Yadong Li, mother Ying Xia,

for their unconditional love,

to my wife, Xiaoai Jiang,

for her unconditional support.

Table of Contents

List of Figures

Acknowledgement

I would like to take this opportunity to express my appreciation to those who have helped me during my graduate student career. First and foremost, I would like to greatly thank my advisor, Professor Xiangfeng Duan, for his continuous help and guidance throughout the entirety of my Ph. D. His constant enthusiasm for scientific research is exceptional. Whenever I discussed my ongoing project or research proposal with him, his keen insight can always give me inspiration to solve scientific problems. I am truly admire his amazing ability to discover critical point in each project, he will always be an academic role model for me.

Secondly, I would like to thank my committee members, Professor Yu Huang, Professor Richard B. Kaner and Professor Alexander M. Spokoyny for their help on my oral qualification exam and final dissertation. Their valuable feedback really helped me understand and improve my deficiencies in graduate research.

Moreover, I would like to appreciate numerous post docs and graduate students that I have worked with. First of all I'd like to thank Dr. Zipeng Zhao for his help on helping me solve many experimental problems. He is always very patient when discussing details and conducting experiments. Second, I'd like to thank my collaborators Dr. Tao Chen from Professor William Andrew Goddard III's group and Dr. Kaining Duanmu from Professor Philippe Sautet's group for their theory computation work. Their diligent work contributed a huge part in my research projects. Finally, I'd like to thank Dr. Zhaoyang Lin, Dr. Chih-Yen Chen, Dr. Xiaoqing Huang, Dr. Enbo Zhu, Dr. Gongming Wang, Dr. Mengning Ding, Dr Xing Zhong and all the other group members and collaborators.

Last but not least, I would greatly thank my parents and my wife for all the love and encouragement. Without your unconditional support, I will not achieve what I have achieved today. It is to them this thesis is dedicated.

VITA

2012	B.S. in Chemistry, Nanjing University, Nanjing
2013	M.S. in Chemistry, University of California, Los Angeles
2016	Faculty Award for Innovation in Inorganic Chemistry
2017	Dissertation Year Fellowship

Chapter 1. Introduction

1.1 Fuel cell and oxygen reduction reaction

Exhaust emission from consumption of nonrenewable fossil fuel has been considered the primary reason responsible for global warming and atmospheric pollution. The continued development of clean energy sources represents the key solution to mitigate these challenges. Proton exchange membrane fuel cell, with renewable hydrogen as fuel and only water as the byproduct, is thought to be a prominent candidate for clean energy supply, especially for ground transportation.[1] Fuel cell system is projected to penetrate the market and grow exponentially in foreseeable future (Fig.1).[2] Recently, fuel cell vehicles such as Toyota Mirai, Hyundai Tucson have already been launched. Compared to current electrical vehicles, which are also representative zero emission transportation tools, fuel cell vehicles show considerable advantage with much shorter refuel time and much longer driving range. Additionally, compared with traditional transportation energy supply (*e.g.*, internal combustion engine or fossil-fuel derived electricity for battery), the fuel cells represent an intrinsically more efficient energy conversion process. Thus fuel cell vehicle represents a future trend as clean energy based transportation.

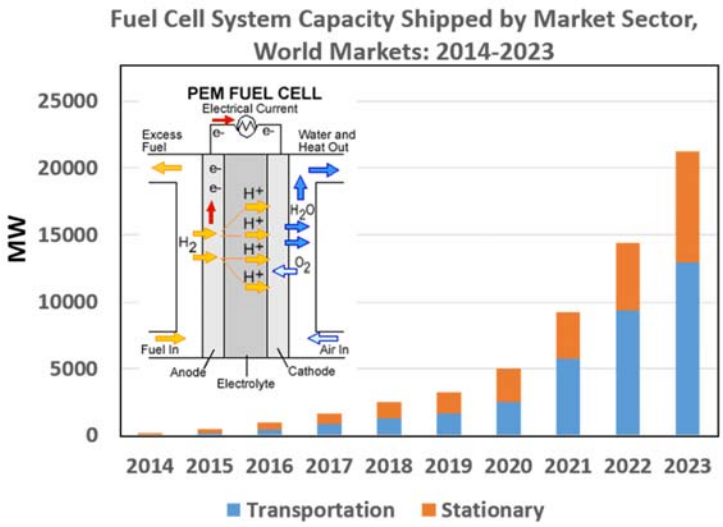

Figure 1.1. Prediction chart of fuel cell system capacity shipped by market sector,[1] the blue, orange section represent fuel cell system in transportation and stationary category respectively. The inset is Schematic diagram of polymer electrolyte membrane (PEM) fuel cells. *Adapted from https://en.wikipedia.org/wiki/Fuel_cell.*

However, the wide spread adoption of fuel cell vehicles is limited by their prices. The basic chemical-electrical energy converting process can be described in a simple formula: $2H_2 + O_2 \rightarrow 2H_2O$ (Fig.1 inset). Fundamentally, the slow kinetics of oxygen reduction reaction is the most critical step limited the performance of a fuel cell.[3] In particular, the need for noble metal catalyst for the sluggish oxygen reduction reaction in fuel cells contributes a significant portion of their high cost. To date, platinum (Pt) is widely recognized as the best element for catalyzing the ORR.[4-8] However, due to its extreme scarcity, the Pt-based catalyst accounts for 55% of fuel cell stack cost.[1] Hence, promoting Pt mass activity (the catalytic activity per given mass of Pt) is central for reducing the cost of fuel cells sufficiently for commercial development.

1.2 Hydrogen evolution reaction

Hydrogen (H_2), with an exceptional energy storage density, is considered as a promising source for green energy and a potential substitution for fossil fuel,[9-12] especially in fuel cell applications. Among all the techniques for H_2 generation, hydrogen evolution reaction (HER) is one of the most investigated reactions in academic field. When consider the media for conducting electro-chemically producing H_2, alkaline water electrolysis is attracting increasing interest for readily accessible reactants, high product purity, and the feasibility for large-scale production, etc.[13-15] Water electrolysis consists of two important half reactions, including the hydrogen evolution reaction (HER) and the oxygen evolution reaction (OER) that typically require precious metal catalysts to reduce the over-potential. The overall of water electrolysis process could be simply described as $2H_2O \rightarrow 2H_2 + O_2$. As shown in the schematic diagram in figure 2, HER happens on cathode side, and this electrochemical processes will consume large amounts of electrical energy without catalyst due to the hydrogen over-potential. Hence, the reduction of cathodic overvoltage is of great interest in attempts to minimize energy consumption.

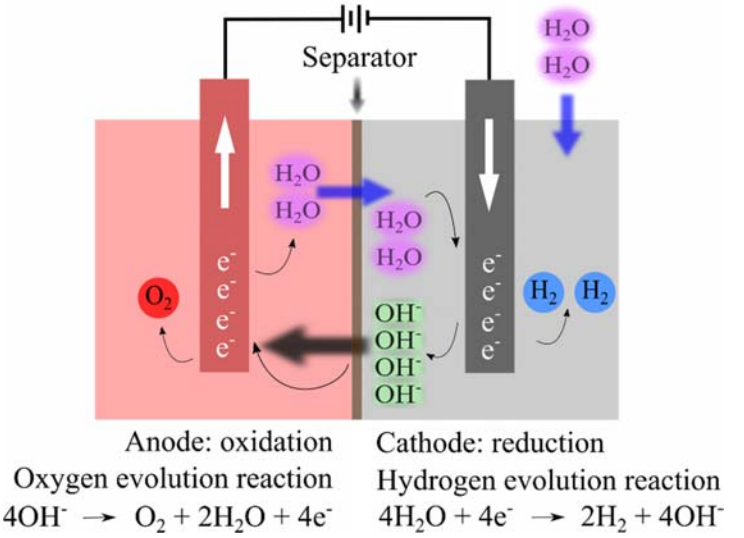

Figure 1.2. The Schematic diagram of alkaline electrolyzer. *Adapted from https://lepa.epfl.ch/page-139282-en.html.*

1.3 Overview of the dissertation

In this dissertation, I will mainly focus on the platinum-based catalyst design for two typical electro-chemical reaction, oxygen reduction reaction and hydrogen evolution reaction.

In chapter 2, I will firstly introduce a solution based synthetic rout combine with an annealing process to produce Ni-rich Pt-Ni alloy nanowires as based material for catalyst design. Next step, an electro-chemical de-alloying approach would be used to produce jagged platinum nanowire as an active ORR catalyst. The ultrafine defective geometry of result J-PtNWs will significantly increase the electrochemically active surface area, and create a compressed surface strain to tune the area specific ORR activity towards optimal value. Characterizations such as high-resolution transmission electron microscopy, inductively coupled plasma, extended X-ray absorption fine structure etc. were used to determine the morphology, composition, coordination environment

information of result nanomaterial. Electro-chemical tests for J-PtNWs and bench mark Pt/C were conduct on rotation disk electrode (RDE) to evaluate the ORR catalytic properties for J-PtNWs material. The specific and mass activity of J-PtNWs at 0.9V versus reversible hydrogen electrode (RHE) were 33 times and 52 times higher than that of Pt/C respectively.

In chapter 3, based on the previous work, we used a cyclic voltammetry decoration method to modify partially de-alloyed J-PtNWs with nickel hydroxide species. Characterizations such as X-ray photoelectron spectroscopy, extended X-ray absorption fine structure, energy-dispersive X-ray spectroscopy etc. were used to confirm the ratio and oxidation state of nickel-related species. The alkaline HER activity of result hybrid nanowire materials were evaluated both on RDE and carbon paper electrode. Commercial Pt/C catalyst was used as bench mark material for comparison. At -0.07 V versus RHE at pH14, the J-PtNWs/$Ni(OH)_2$ exhibits a record high 17 times higher HER mass activity compare with Pt/C.

1.4 References

1. Bing, Y.; Liu, H.; Zhang, L.; Ghosh, D.; Zhang, J. Nanostructured Pt-alloy electrocatalysts for PEM fuel cell oxygen reduction reaction. *Chem. Soc. Rev. 39*, 2184-2202 (2010).

2. Christensen, K. Fuel cell industry shows potential. *http://seekingalpha.com/article/2859906-fuel-cell-industry-shows-potential* (2015).

3. Kongkanand, A.; Mathias, M. F. The priority and challenge of high-power performance of low-platinum proton-exchange membrane fuel cells. *J. Phys. Chem. Lett.*, 7, 1127-1137 (2016).

4. Zhang, L.; Xie, Z.; Gong, J. Shape–controlled synthesis of Au–Pd bimetallic nanocrystals for catalytic applications. *Chem. Soc. Rev.*, 45, 3916-3934 (2016)

5. Markovic, N.; Schmidt, T.; Stamenkovic, V.; Ross, P. Oxygen reduction reaction on Pt and Pt bimetallic surfaces: a selective review. *Fuel Cells*, 1, 105-116 (2001)

6. Schmidt, T.; Paulus, U.; Gasteiger, H.; Behm, R. The oxygen reduction reaction on a Pt/carbon fuel cell catalyst in the presence of chloride anions. *J. Electroanal. Chem.*, 508, 41-47 (2001)

7. Gasteiger, H. A.; Kocha, S. S.; Sompalli, B.; Wagner, F. T. Activity benchmarks and requirements for Pt, Pt-alloy, and non-Pt oxygen reduction catalysts for PEMFCs. *Appl. Catal. B* 56, 9-35 (2005)

8. Peng, Z.; Yang, H. Designer platinum nanoparticles: control of shape, composition in alloy, nanostructure and electrocatalytic property. *Nano Today*, 4, 143-164 (2009)

9. Dresselhaus, M. & Thomas, I. Alternative energy technologies. *Nature* 414, 332 (2001).

10. Vesborg, P. C., Seger, B. & Chorkendorff, I. Recent development in hydrogen evolution reaction catalysts and their practical implementation. *J. Phys. Chem. Lett,* 6, 951-957 (2015).

11. Turner, J. A. Sustainable hydrogen production. *Science* 305, 972-974 (2004).

12. Jacobson, M., Colella, W. & Golden, D. Cleaning the air and improving health with hydrogen fuel-cell vehicles. *Science* 308, 1901-1905 (2005).

13. Gandía, L. M., Oroz, R., Ursúa, A., Sanchis, P. & Diéguez, P. M. Renewable hydrogen production: performance of an alkaline water electrolyzer working under emulated wind conditions. *Energy & Fuels* 21, 1699-1706 (2007).

14. Kong, D., Wang, H., Lu, Z. & Cui, Y. CoSe2 nanoparticles grown on carbon fiber paper: an efficient and stable electrocatalyst for hydrogen evolution reaction. *J. Am. Chem. Soc* 136, 4897-4900 (2014).

15. Zheng, Y. et al. Toward design of synergistically active carbon-based catalysts for electrocatalytic hydrogen evolution. *ACS nano* 8, 5290-5296 (2014).

Chapter 2. Ultrafine jagged Pt nanowires for oxygen reduction reaction

2.1 Introduction

Platinum (Pt) represents the essential element for catalyzing the oxygen reduction reaction (ORR),[1-3] However, the catalyzed ORR rate is still slow enough that the high cost of Pt becomes the limiting factor preventing the widespread adoption of fuel cells,[4,5] and higher Pt mass activity (the catalytic activity per given mass of Pt) must be achieved. The Pt mass activity is determined by the specific activity (SA, normalized by surface area) and the electrochemically active surface area (ECSA, normalized by mass). The SA can be optimized by tuning the chemical environment, including chemical composition,[6-9] exposed catalytic surface,[1, 10-12] and Pt coordination environment.[13-16] To date, the highest SAs has generally been achieved on single crystal surfaces or well-defined nanoparticles (NPs) with specifically engineered facet structure and alloy compositions. For example, the Pt_3Ni (111) single crystal facet[1] and subsequently Pt_3Ni octahedral NPs exhibit ORR-favorable surface structure for greatly enhanced activity,[17-19] but such alloys typically suffer from insufficient stability because of electrochemical leaching of Ni during electrochemical cycling and decreased ECSA because of agglomeration of the NPs. Introduction of Mo surface dopants can minimize such leaching processes and help maintain the ORR-favorable Pt_3Ni (111) surface for enhanced activity and stability.[19] Although high SA has been achieved on these structures, the reported ECSA for these optimized structures are typically limited to ~ 70 $m^2/_{gPt}$. However, the ECSA has been improved by tailoring the geometrical factors including creating ultrafine nanostructures[20, 21] or core/shell nanostructures with an ultrathin Pt skin that exposes most Pt atoms on the surface.[22-24]

To boost both Pt mass activity and Pt utilization efficiency, an ideal catalyst should have an ORR-favorable chemical environment for high SA, an optimized geometric factors for high ECSA,[20-24] and a system that maintains these high values for long periods of operation. We report the preparation of ultrafine jagged Pt nanowires (J-PtNWs) (diameter ~2.2 nm) with rich ORR-favorable rhombic configurations to lead to an SA of 11.5 mA/cm^2 (at 0.9 V *vs.* RHE: reversible hydrogen electrode) and an ECSA of 118 m^2/g$_{Pt}$. Together, these J-PtNWs deliver mass activity of 13.6 A/mg$_{Pt}$ (at 0.9 V *vs.* RHE), which is ~50 times higher than state-of-the-art commercial Pt/C catalyst, and that nearly doubles the highest mass activity values previously reported of 6.98 A/mg$_{Pt}$[19] and 5.7 A/mg$_{Pt}$.[23] Finally, the PtNi alloy NWs were electrochemically dealloyed to produce ultrafine pure Pt NWs with jagged surfaces. Here, Ni does not play an active electronic or structural role but is sacrificial, as it is leached entirely to form ultrafine pure J-PtNWs.

2.2 Nanowire synthesis and characterizations

Preparation of Pt/NiO NWs and Pt-Ni nanowire catalysts

In a typical synthesis, 0.025 mmol Pt(acac)$_2$, 0.10 mmol Ni(acac)$_2$ and 0.75 mmol glucose were pre-dissolved in mixture of 2 mL 1-octadecene (ODE) and 3 mL oleylamine (OAm). After sonicated for 10 min, 0.0015 mmol PVP (mw. 40,000) and 0.0050 mmol W(CO)$_6$ were added into the pre-dispersed solution and sealed with argon. The mixture was further heated up to 140 ^{o}C for 6 hours to obtain Pt/NiO core/shell nanowires, which were then washed and cleaned using acetone/cyclohexane/ethanol mixture, and collected by centrifuging at 7000 rpm.

The as-prepared Pt/NiO NWs were suspended in 15 mL cyclohexane/ethanol mixture. To load the sample on to carbon black, 36 mg of carbon black was added for each 4 mg Pt/NiO NWs and

sonicated for 2 hours. The resulting Pt/NiO-NWs/C catalysts were collected by centrifugation and cleaned with cyclohexane/ethanol mixture, placed in an alumina boat and annealed at 450 ^{o}C in Ar/H_2: 97/3 with 100 sccm flow rate in a home-build tube furnace.

Preparation of regular Pt nanowire (R-PtNW) catalysts

In a typical synthesis, 0.025 mmol platinum $Pt(acac)_2$, 0.10 mmol $Co(acac)_2$ and 0.75 mmol glucose were pre-dissolved in mixture of 2 mL 1-octadecene (ODE) and 3 mL oleylamine (OAm). After sonicated for 10 min, 0.0015 mmol PVP (mw. 40,000) and 0.0050 mmol $W(CO)_6$ were added into the pre-dispersed solution and sealed with argon. The mixture was further heated up to 120 ^{o}C for 3 hours to get regular nanowires. After cleaned the product by acetone/cyclohexane/ethanol mixture, the R-PtNWs were collected by centrifuging at 7000 rpm, and re-suspended in 15 mL cyclohexane/ethanol mixture and loaded onto carbon black using the same approach described above, flowed by a moderate annealing at 250 ^{o}C.

Preparation of Pt-Ni nanoparticles

In a typical synthesis, 0.025 mmol platinum $Pt(acac)_2$, 0.075 mmol $Ni(acac)_2$ and 0.75 mmol glucose were pre-dissolved in mixture of 2 mL 1-octadecene (ODE) and 3 mL oleylamine (OAm). After sonication for 10 min, 0.0015 mmol PVP (mw. 40,000) and 0.050 mmol $W(CO)_6$ were added into the pre-dispersed solution and sealed with argon. The mixture was further heated up to 170 ^{o}C for 6 hours with stirring to obtain PtNi nanoparticles (NPs). After cleaning with a mixture of acetone/cyclohexane/ethanol, the PtNi NPs were collected by centrifuging at 12,000 rpm, and re-suspended in 15 mL cyclohexane/ethanol mixture and loaded onto carbon black using the same approach described above, flowed by a thermal annealing at 450 ^{o}C.

Preparation of Pt-Co nanowires

In a typical synthesis, 0.025 mmol platinum $Pt(acac)_2$, 0.100 mmol $Co(acac)_2$ and 0.75 mmol glucose were pre-dissolved in mixture of 2 mL 1-octadecene (ODE) and 3 mL oleylamine (OAm). After sonication for 10 min, 0.0015 mmol PVP (mw. 40,000) and 0.0050 mmol $W(CO)_6$ were added into the pre-dispersed solution and sealed with argon. The mixture was further heated up to 170 ^oC for 6 hours with stirring to obtain Pt/Co core/shell nanowires (NWs). After cleaning with a mixture of acetone/cyclohexane/ethanol, the Pt/Co core/shell nanowires were collected by centrifuging at 12,000 rpm, and re-suspended in 15 mL cyclohexane/ethanol mixture and loaded onto carbon black using the same approach described above, flowed by a thermal annealing at 450 ^oC.

Characterizations

Transmission electron microscopy (TEM) studies show that the as-synthesized NWs exhibit an apparent core/shell structure with a higher contrast core and lower contrast shell. The NWs have a typical overall diameter ~ 5 nm or less, and a length between about 250 to 300 nm (Fig.2.1 A, Fig. 2.2 A). High-resolution TEM (HRTEM) studies confirm the core/shell structure with a typical core diameter of 2.0 nm ± 0.2 nm (Fig. 2.2D). The shell shows well-resolved lattice fringes with the spacing of 0.24 nm, corresponding to the (111) lattice planes of face-centered cubic (fcc) NiO (Fig. 2.2D), and the core displays a primary lattice spacing of 0.23 nm, corresponding to Pt (111) planes (Fig. 2.2D).

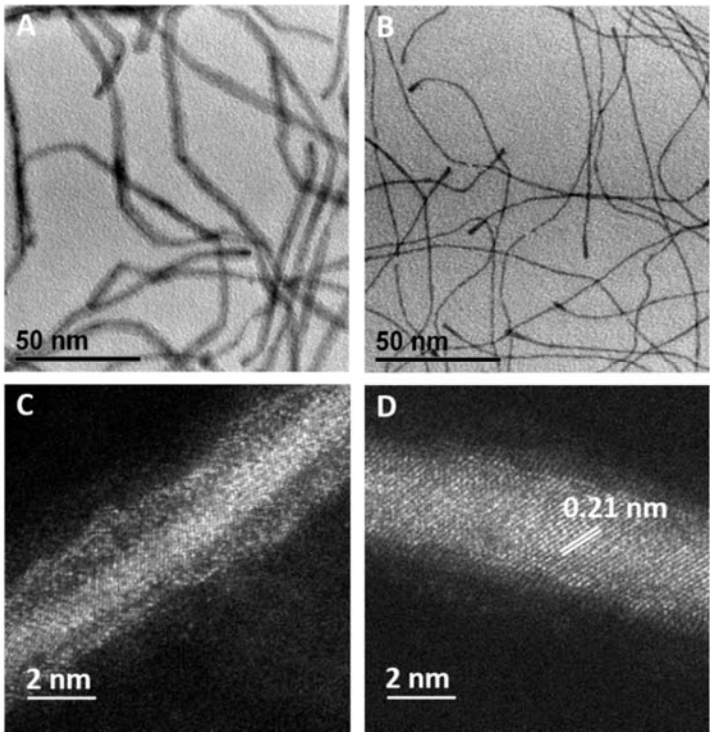

Figure 2.1. (**A** and **B**) TEM images for Pt/NiO core/shell nanowires and regular nanowires. (**C** and **D**) STEM images for Pt/NiO nanowires/C before and after annealing at 450 ^{o}C in Ar/H_2 (97/3) atmosphere for 12 hours.

These Pt/NiO NWs were then loaded onto carbon black and annealed in an argon/hydrogen mixture (Ar/H_2: 97/3) at 450^{o}C to produce PtNi alloy NWs. The overall morphology of the NW was maintained without obvious change in length or diameter, but the apparent core/shell contrast disappeared (Fig. 2.2B), suggesting the formation of uniform PtNi alloy NWs.

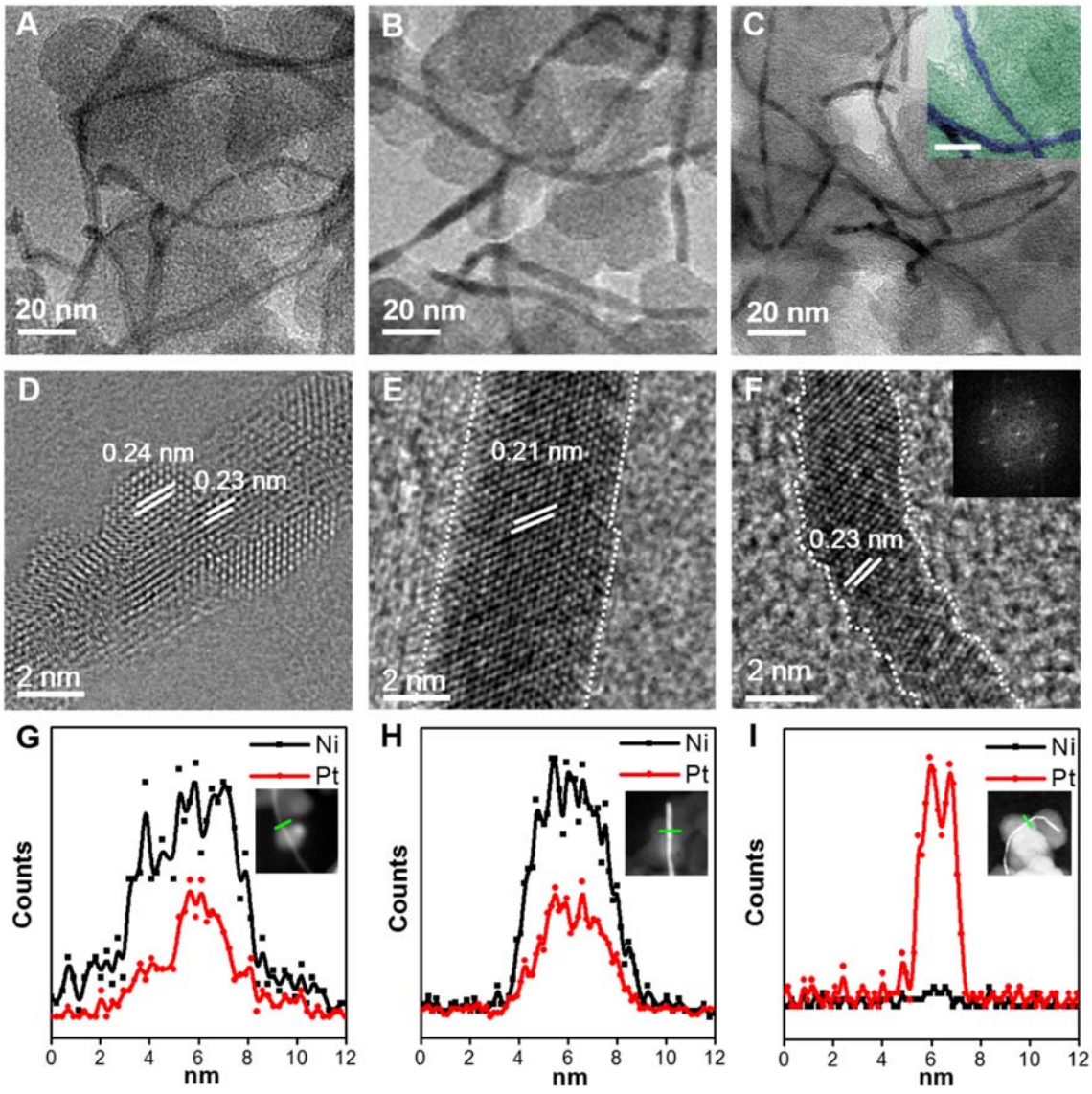

Figure 2.2. Structure and composition characterization of different stages of the J-PtNW evolution process. (**A, B** and **C**) Representative TEM images and (**D, E** and **F**) HRTEM images of the Pt/NiO core/shell NWs, the PtNi alloy NWs and the J-PtNWs supported on carbon, respectively. The inset in **C** shows a false-colored, zoomed-in image of the J-PtNWs, highlighting the rough surface (scale bar: 10 nm). The inset in **F** shows the corresponding FFT image. The dashed lines in **E** and **F** show the outline of the NWs, highlighting the rough surface of the J-

PtNWs. (**G, H** and **I**) EDS line-scan profiles of the corresponding NWs show clearly the evolution from the Pt/NiO core/shell, to PtNi alloy, and then pure Pt NWs.

We believe that the NW geometry is essential for ensuring the thermal stability of these ultrafine NWs under high temperature annealing compared with NPs. For example, a similar thermal annealing process applied to ultrafine PtNi NPs led to substantial aggregation of the NPs (a size increase from ~ 7 nm before to 10 to 30 nm) (Fig. 2.3) that could be partly attributed to the movement and fusion of NPs. In contrast, NWs supported on carbon black have multiple anchoring points and the mobility of the NWs on carbon support is much lower compared to NPs with single point contact.

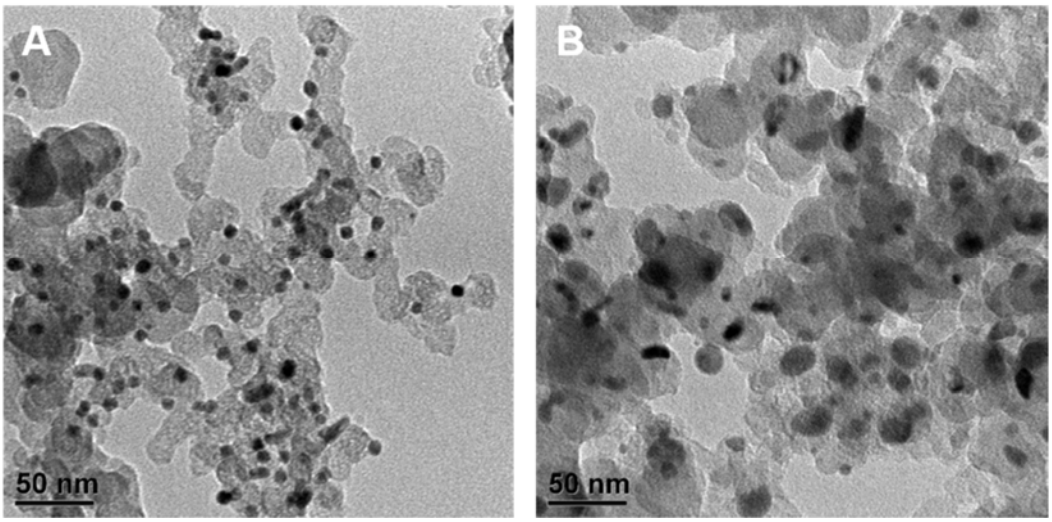

Figure 2.3. TEM images of PtNi NPs (**A**) before and (**B**) after annealing at 450 ^{o}C in Ar/H_2 (97/3) atmosphere for 12 hours.

Our energy-dispersive x-ray spectroscopy (EDS) elemental analysis shows that the overall Pt/Ni ratio remains essentially the same (Pt/Ni: 15/85) before and after annealing (Fig. 2.4 A, B). The HRTEM image of the annealed NW shows a uniform contrast with a well-resolved lattice

spacing of 0.21 nm throughout the entire NW diameter (Fig. 2.2 E), consistent with the (111) lattice spacing of the PtNi alloy.

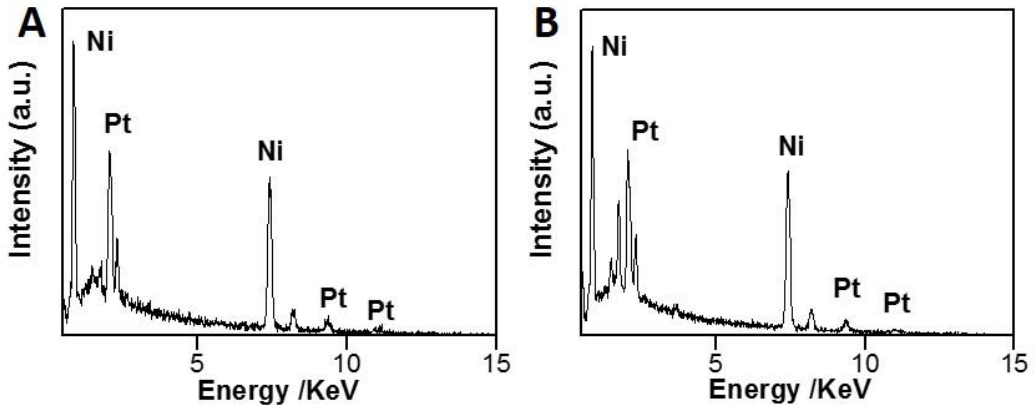

Figure 2.4. EDS spectrum of (**A**) as-prepared Pt/NiO core/shell NWs. (**B**) Pt-Ni alloy NWs obtained after 450 ^{o}C annealing.

This evolution from the initial core/shell NWs before annealing to uniform alloy NWs after annealing was also confirmed by high-angle annular dark-field scanning transmission electron microscope (HAADF-STEM) studies (Fig. 2.1 C, D). The EDS line scan profile of the as-prepared NWs also confirms the core/shell structure with a Pt core (Fig. 2.2 G) that diffuses homogenously throughout the entire NW after annealing (Fig. 2.2 H). X-ray diffraction (XRD) studies also confirm the evolution of the initial Pt/NiO core/shell configurations into a fully alloyed PtNi NW structure (Fig. 2.5).

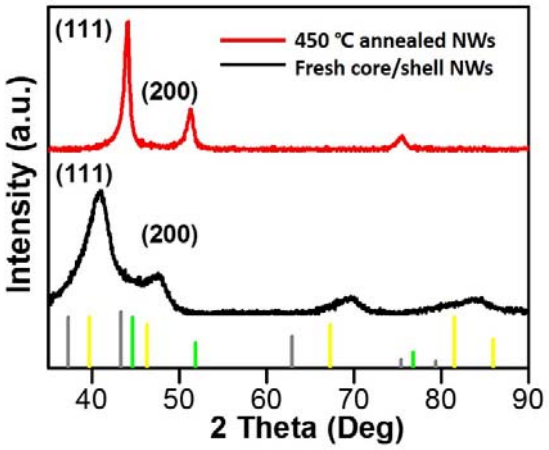

Figure 2.5. XRD spectra comparison of fresh and 450 °C annealed Pt/NiO core/shell nanowires/C. The standard XRD pattern for *fcc* NiO, Pt, Ni are displayed as grey, yellow, and green bars. The crystallinity of fresh sample (black line) showed existence of non-*fcc* phase, and since the size of Pt core NWs is ultrafine (sub 2 nm), the result XRD peak for fresh sample is broadened. The overlapped (111) and (200) peak region could be caused by the existence of NiO. For 450 °C annealed sample (red line), the narrowed symmetric XRD peak suggested the formation of larger alloyed crystal. The result (111) peak ($2\theta = 44.0^{o}$) was relatively closer to Ni (111) ($2\theta = 44.6^{o}$) than that of Pt (111) ($2\theta = 39.7^{o}$), indicates the result alloy is Ni-rich which is constant with our EDS result (Fig. S3B).

Furthermore, x-ray photoelectron spectroscopy (XPS) studies further demonstrate that the nickel valence state changed from Ni^{x+} in the Pt/NiO core/shell NWs to mostly Ni^{0} after annealing, consistent with the formation PtNi alloy (Fig. 2.6).

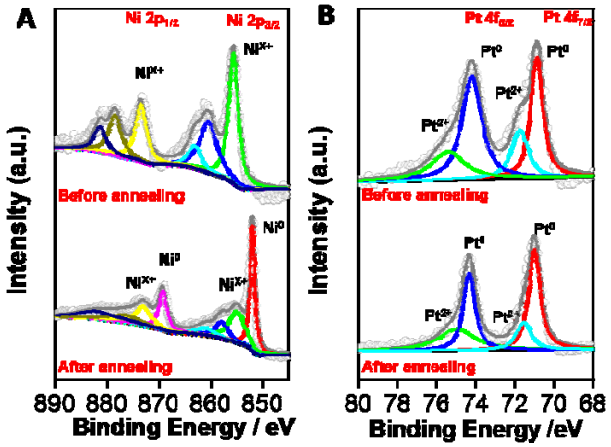

Figure 2.6. XPS spectra comparison before and after annealing of Pt/NiO core/shell nanowires/C. (**A**) Ni 2P, (**B**) Pt 4f.

2.3 Oxygen reduction reaction properties

An electrochemical de-alloying (leaching) process was used to gradually remove Ni atoms from the PtNi alloy NWs, which allowed the rearrangement of Pt atoms on surface to form the J-PtNWs. We performed cyclic voltammetry (CV) in N_2-saturated 0.1 M $HClO_4$ solution (0.05 V to 1.1 V *vs.* RHE) with a sweep rate of 100 mVs^{-1} (Fig. 2.7 A). Based on the CV sweeps, the $ECSA_{Hupd}$ was derived from the H_{upd} adsorption/desorption peak areas (0.05 V < E < 0.35 V) and the total mass of the loaded Pt. The PtNi alloy NWs initially showed an essentially negligible $ECSA_{Hupd}$ during the first CV cycle. The $ECSA_{Hupd}$ increased steadily with the increasing number of CV cycles (Fig. 2.7 B). Importantly, the NWs were fully activated in ~ 160 CV cycles to reach a stable $ECSA_{Hupd}$ up to 118 cm^2/mg_{Pt}, versus previous highest reported values of ~70 cm^2/mg_{Pt} (Table 2.1).

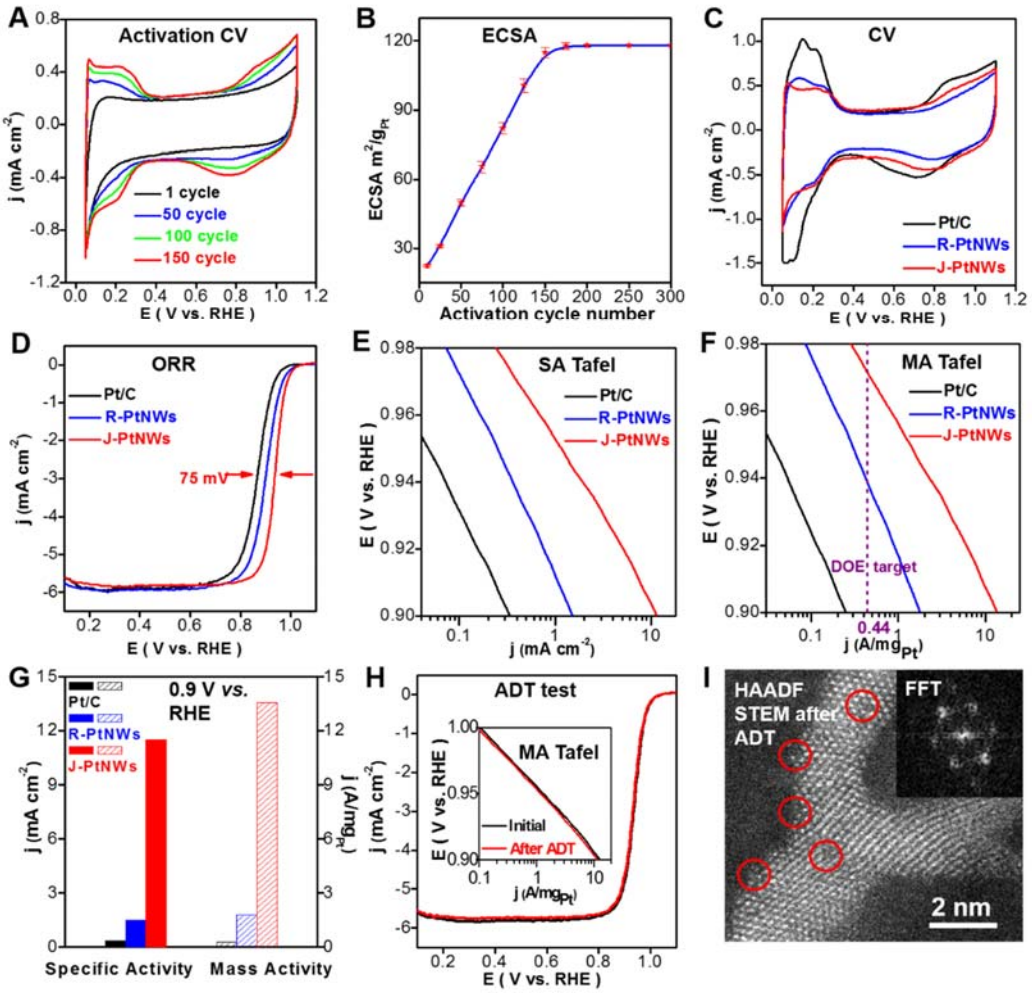

Figure 2.7. Electrochemical performance of the jagged PtNWs (J-PtNWs) vs. regular synthetic PtNWs (R-PtNWs) and commercial Pt/C. (**A**) Cyclic voltammetry (CV) curves corresponding to different activation cycles of the de-alloying process, clearly indicating the increasing surface area with the increasing number of CV cycles. (**B**) The evolution of ECSA with the increasing CV cycles, showing that 150 cycles are sufficient to construct the J-PtNW and reach a stable ECSA. (**C** and **D**) CV and ORR polarization curves for the J-PtNWs, the R-PtNWs, and the Pt/C, respectively. (**E** and **F**) Specific activity (SA) and mass activity (MA) Tafel plot for the J-PtNWs, the R-PtNWs, and the Pt/C, respectively. The purple dash line indicates the 2017 mass activity target (@ 0.90V vs. RHE) set by US Department of Energy (DOE). (**G**) The comparison

of specific activities and mass activities of the J-PtNWs, the R-PtNWs, and the Pt/C at 0.9 V *vs.* RHE, showing that the J-PtNWs deliver 52 times higher mass activity or 33 times higher specific activity than Pt/C, potentially reducing materials costs by a factor up to 52. (**H**) ORR polarization curves and mass activity Tafel plot (inset) for the J-PtNWs before and after 6000 CV cycles between 0.6 and 1.0 V versus RHE, showing little loss in activity. The scan rate for the Accelerated Durability Test (ADT) is 100 mVs^{-1}. (**I**) High-resolution HAADF-STEM image of the J-PtNWs after ADT test. The circled areas indicate defective regions with missing atoms. The inset shows the corresponding FFT image.

Table 2.1. Electrochemically active surface area, specific activity, half-wave potential and mass activity of J-PtNWs/C, R-PtNWs/C, Pt/C catalysts, in comparison with those in several representative recent studies.

	ECSA (m^2/g_{Pt})	**SA (mA/cm^2) @ 0.90 V**	**Half-wave potential (V)**	**Mass activity (A/mg_{Pt})**	
				@ 0.90 V	**@ 0.935 V**
J-PtNWs/C (this work)	118	11.5	0.935	13.6	2.87
R-PtNWs/C (this work)	110	1.59	0.899	1.76	0.5
Pt/C (this work)	74	0.35	0.860	0.26	0.06
Octahedron $Pt_{2.5}Ni/C$ (*ref.17*)	21	NA	NA	3.3	NA
Nanoframe Pt_3Ni/C (*ref.23*)	67.2	NA	NA	5.7	NA
Mo-Pt_3Ni/C (*ref.19*)	67.7	10.3	NA	6.98	NA
DOE 2017 target	NA	NA	NA	0.44	NA

Structural and elemental studies were performed to characterize the fully activated NWs after CV cycles. Low-resolution TEM images show that the overall NW structure was well-maintained after the electrochemical (or CV) de-alloying process (Fig. 2.2 C). The HRTEM images show that the overall diameter of the NW shrank from ~ 5.0 to ~ 2.2 nm after the CV cycles, with well-resolved lattice spacing of 0.23 nm, again consistent with Pt (111) (Fig. 2.2 F). The EDS line scan showed that only Pt was present in the resulting NWs (Fig. 2.2 I), further confirming complete Ni leaching. In addition, the CV scan of the fully activated NWs (after 160 CV cycles) in 0.1 M KOH showed an absence of typical Ni^{2+}/Ni^{3+} redox signatures, in contrast to the partially activated (150 cycles) PtNi alloy NWs in which the Ni^{2+}/Ni^{3+} redox peaks were prominent (Fig. 2.8).

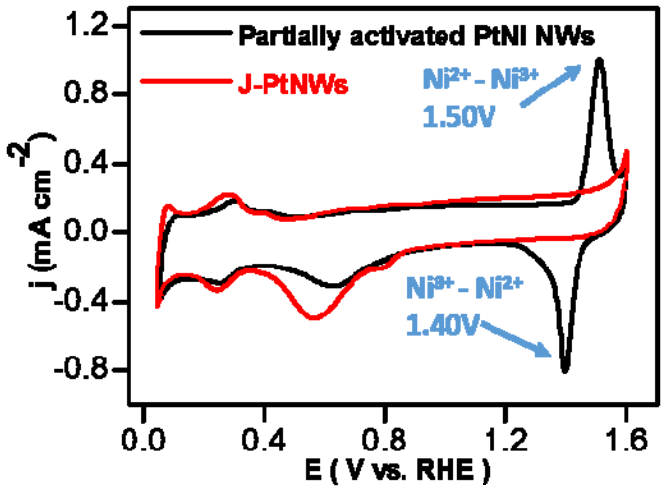

Figure 2.8. The cyclic voltammetry (CV) curves for partially activated Pt-Ni alloy NWs (150 cycles in 0.1 M HClO4 solution) and J-PtNWs in alkaline electrolyte with scan rate of 50 mVs^{-1}. The current densities were normalized to the geometric area of the RDE (0.196 cm^2).

We also conducted CO-stripping to determine the $ECSA_{CO}$ of J-PtNWs (Fig. 2.9). The resulting ratio of $ECSA_{Hupd}$: $ECSA_{CO}$ is 1.00:1.05, which is in agreement with that of typical pure Pt material.[22] Furthermore, TEM studies of the de-alloyed NWs also showed a highly jagged

surface (Fig. 2.2, C and F) with rich atomic steps, in contrast to relatively smooth surface observed in typical synthetic PtNWs (Fig. 1.1 B). Based on these observations, we denote the resulting nanowires as the jagged PtNWs (J-PtNWs).

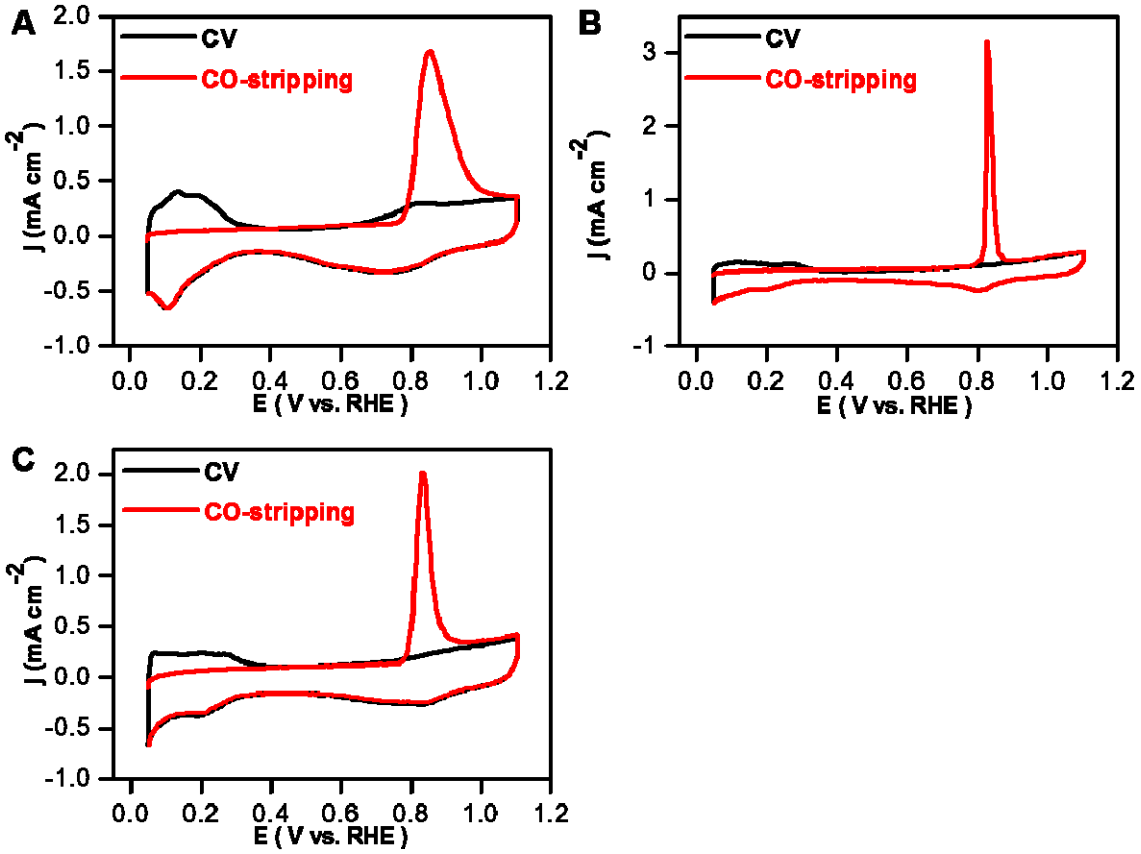

Figure 2.9. The CV and CO-stripping curves of the (**A**) Pt/C, (**B**) R-PtNWs, and (**C**) J-PtNWs. All the CO-stripping curves were recorded at room temperature in CO-saturated 0.1 M $HClO_4$ solution at scan rate of 50 mVs^{-1}. The current densities were normalized to the geometric area of the RDE (0.196 cm^2). The $ECSA_{Hupd}$: $ECSA_{CO}$ ratio is 1:1.03, 1:1.06, 1:1.05 for Pt/C, R-PtNWs, J-PtNWs repectively.

The electrocatalytic performance of the resulting NWs was compared with commercial Pt/C catalyst (10 % mass loading of ~ 3 to 5 nm Pt NPs on carbon support) and directly synthesized

regular PtNWs (R-PtNWs, ~ 1.8 nm diameter, Fig. 1.1 B) with relatively smooth surface (the synthesis method is described in supplementary materials, SM). To assess the ORR activity, all catalysts were loaded onto glassy carbon electrodes (Pt mass loading: 2.2 μg/cm^2 for J-PtNWs, 2.55 μg/cm^2 for R-PtNWs and 7.65 μg/cm^2 for Pt/C catalyst). We used CV to measure the ECSA (Fig. 2.7 C). Overall, the J-PtNWs, R-PtNWs and Pt/C catalysts showed an ECSA of 118, 110, and 74 m^2/g_{Pt}, respectively (Table 2.1). The synthetic R-PtNWs also exhibited a rather high ECSA that may be related to their ultrasmall diameters (~ 1.8 nm).

Fig. 2.7 D shows the ORR polarization curves normalized by glassy carbon electrode geometric area (0.196 cm^2). The half-wave potential for the J-PtNWs was at 0.935 V, which is considerably higher than those of the commercial Pt/C (0.86 V) and the R-PtNWs (0.90 V), suggesting excellent ORR activity of the J-PtNWs. The Koutecky-Levich equation was used to calculate the kinetic current by considering the mass-transport correction. The specific and mass activities were normalized by the ECSA or the total mass of the loaded Pt, respectively. Overall, the J-PtNWs showed a specific activity of 11.5 mA/cm^2 at 0.90 V *vs.* RHE, far higher than 0.35 mA/cm^2 for the Pt/C or 1.70 mA/cm^2 for the R-PtNWs tested under the same conditions. Together with their ultrahigh specific surface area, the J-PtNWs deliver a high mass activity of 13.6 A/mg_{Pt} at 0.9 V *vs.* RHE, which is 52 times higher than that of the 10 % wt Pt/C (0.26 A/mg_{Pt}), and more than 7 times higher than that of the R-PtNWs (1.76 A/mg_{Pt}) (Fig. 2.7 G) (Table 2.1). The mass activity achieved in the J-PtNWs nearly doubles the highest mass activity value previously reported of 6.98 A/mg_{Pt} [19] and 5.7 A/mg_{Pt} [23]. Also, the observed mass activity was highly reproducible and was between 10.8 and 13.8 A/mg_{Pt} in >15 independently tested J-PtNW electrodes.

Because the current value at 0.90V is already near the diffusion-limited current in ORR polarization curve, we also compared mass activity at half-wave potential of the J-PtNWs (0.935 V) in Table 2.1. Our analysis shows that the J-PtNWs still exhibit an impressive 48 times higher mass activity than that of Pt/C. The specific activity Tafel plots (Fig. 2.7 E) exhibit a slope of 51, 72 and 74 mV dec^{-1} for J-PtNWs, R-PtNWs and Pt/C, respectively. A considerably smaller slope achieved in the J-PtNWs suggests significantly improved kinetics for oxygen reduction reaction. Remarkably, the mass activity Tafel plot (Fig. 2.7 F) shows that the J-PtNWs deliver 30 times higher mass activity than the 2017 target set by US Department of Energy (0.44 A/mg_{Pt} at 0.90 V for MEA, highlighted by purple dash line in Fig. 2.7 F). The J-PtNW can deliver the DOE targeted mass activity at 0.975 V (RHE), thus significantly reducing the overpotential by 0.075 V.

We evaluated the durability of the J-PtNWs using accelerated deterioration tests (ADT) under a sweep rate of 100 mVs^{-1} between 0.6 V and 1.0 V in O_2-saturated 0.1 M $HClO_4$. After 6000 cycles, the ECSA dropped only by ~7 %, and the specific activity dropped by only ~5.5 %, and together the mass activity dropped by only 12 % (Fig. 2.7 H). The retention high ECSA in J-PtNWs during ADT can be compared to that of Pt/C, which showed a much larger loss (~30%) in ECSA during similar ADT tests. Ultrafine nanostructures (*e.g.*, ~ 2 nm) have shown severely worse stability compared to their bulk counterpart.[25, 26]The nanowires that allow multipoint support contacts might also deter the Ostwald ripening process usually observed in spherical NPs (Fig. 2.10).

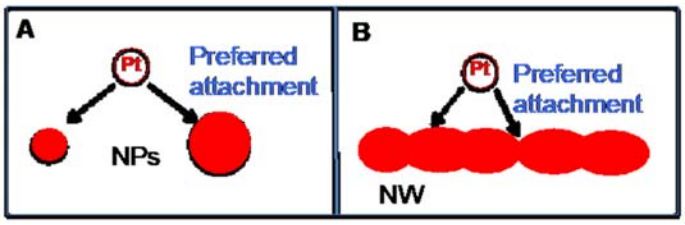

Figure 2.10. Schematic illustration of the difference in Ostwald ripening in 0D NPs vs. 1D NWs. Ostwald ripening in which Pt atoms are dissolved from one nanostructure and reattach to another one, can often lead to aggregation of ultrafine nanostructures. In such processes, the dissolved Pt atoms tend to reattach at new locations that are more energetically favorable, such as locations with smaller curvature or more coordinated neighbors. In this scenario the energetically more favorable sites for NPs are likely NPs with larger size because of smaller curvature (larger radius of curvature) (A), leading to Ostwald ripening and serious loss of ECSA. However, for 1D NWs, the energetically favorable sites are more likely located at the narrower constriction region with negative curvature (B), which would promote atom attachment to the narrow regions and prevent the breakup of 1D structure and thus lead to further stabilization of 1D NW structure.

Indeed, our TEM studies before and after ADT test showed little change in the overall morphology or size of the J-PtNWs on carbon support (Fig 2.11). High-resolution STEM studies showed that the jagged surface (with defective sites) was largely preserved after 6000 cycles (Fig. 2.7 I). The J-PtNWs exhibit higher specific activity and mass activity (11.5 mA/cm^2 or 13.6 A/mg$_{Pt}$ at 0.9 V) than those of R-PtNWs (1.70 mA/cm^2 or 1.87 A/mg$_{Pt}$ at 0.9 V), despite similar ECSA values (118 m^2/g$_{Pt}$ for 2.2 nm J-PtNWs and 110 m^2/g$_{Pt}$ for 1.8 nm R-PtNWs). Compared with Pt/C, the J-PtNWs show a 33 times increase in specific activity at 0.90 V vs. RHE,m which suggests that the activation energy for the rate-determining step of ORR on the J-PtNWs is reduced by 0.090 eV from that of Pt/C [$\Delta E_{act}=k_BT\ln(SA_{J\text{-}PtNW}/SA_{Pt/C})$](ΔE_{act} *:* different activation energy, k_B*:*

Boltzmann's constant, *T:* temparature, $SA_{J\text{-}PtNW}$: specific activity of J-PtNWs, $SA_{Pt/C}$: specific activity of Pt/C) [define all terms here]. This decrease is plausible decrease based on our various ORR computations.[16]

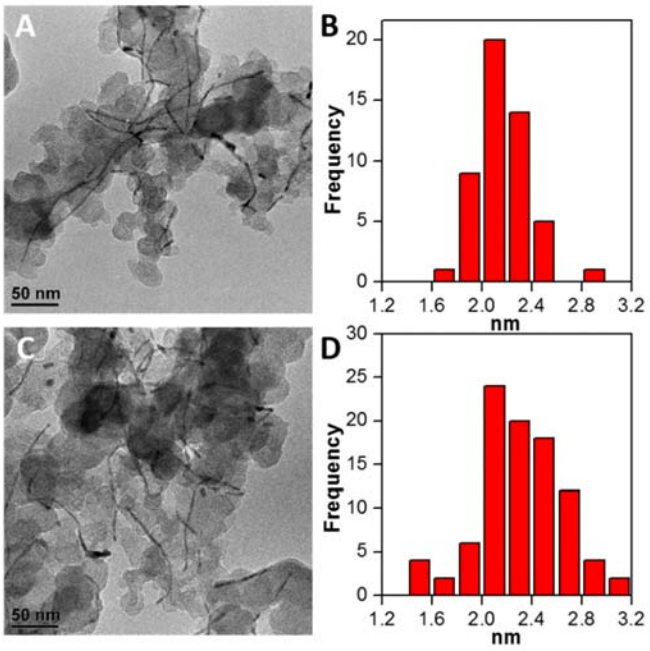

Figure 2.11. (**A**, **C**) TEM images, and (**B**, **D**) NW diameter distribution chart of J-PtNWs after CV activation and ADT test, respectively.

2.4 Simulation results

Computational methods

To generate realistic structural models of PtNi alloy nanowires, we extended the computational protocol developed previously to simulate Ni de-alloying of Pt_3Ni_7 nanoparticles (0D systems).[16]

Thus:

1. We started from an infinite nanowire (1D system), based on the *fcc* Pt crystal structure. The *z* axis of the nanowire is along the (111) crystal direction, while in the *xy* plane we have 13 Pt atoms along the *x* axis and 9 Pt atoms are along the *y* axis. This choice was made to expose some (100) facets along the NW axis
2. We built a periodic model by replicating 220 individual unit cells along the axis of the wire
3. The overall ratio of Ni to Pt is 85: 15 consistent with experiment, which was achieved by randomly replacing 85% of the Pt atoms with Ni atoms, while ensuring that the Ni composition is roughly constant along the nanowire axis.
4. We erase all the Ni atoms and perform a fixed-cell conjugate-gradient local relaxation using the ReaxFF force field. Here at each conjugate-gradient step limits the maximum change in Cartesian coordinates to 0.1 Å to ensure a smooth local minimization that avoids disruption of the original random *fcc* framework. The convergence threshold criteria are 4×10^{-6} eV on the energy and 4×10^{-8} eV/Å on the gradient.
5. We perform a second local relaxation allowing the cell dimension in the z-direction to equilibrate at a pressure of 1 atm.
6. We perform a final NPT Molecular Dynamics (MD) simulation at 343 K for 520 ps (20 ps equilibration followed by a 500 ps run
7. We delete the least coordinated atoms which would be further leached away during ORR cycling and perform an additional NPT Molecular Dynamics (MD) simulation at 343 K for 520 ps (20 ps equilibration followed by a 500 ps run)
8. We locally relax the final structure using a SMA force field.

This protocol, in which we simultaneously remove Ni throughout the initial *fcc* nanostructure and locally relax and equilibrate the resulting configuration, is intended as a simplified mimic of

the complex kinetics-driven de-alloying process induced by during electrochemical activation, where Ni surface atoms are progressively leached out of the system. The ReaxFF reactive force could be used in a more realistic gradual depletion of the Ni atoms under realistic conditions, but the size of the system and the long time scales of ORR-induced de-alloying makes this more realistic simulation impractical. However, we consider that the smooth local minimization of the initial randomly sparse *fcc* framework of Pt atoms provides a reasonable approximation to the relaxation processes through metastable configurations that retain memory of the original pattern. Our assumption that all Ni atoms are removed in step (4), corresponds in our previous nanoparticle study to propagating the topmost 4/6 surface layers devoid of Ni into the bulk.[16] We consider that the experimental evidence showing that all Ni atoms are leached out in these small diameter nanowires fully justifies this approach. It can be noted that the ReaxFF reactive force field[27] has been derived from extensive quantum mechanics calculations validated by comparing to experiment and is used in the process generating structure and overall morphology of dealloyed NWs in which directionality terms in the potential are important. However, this force field tends to overestimate surface distances so that the SMA potential[28] was finally used to compare with experimental data from extended x-ray absorption fine structure (EXAFS) analysis.

We compare the nanowire structural characteristics with those of the Pt_3Ni_7 nanoporous particle obtained by de-alloying a 10-nm-diameter *fcc* Pt_3Ni_7 nanoparticle as a representative nanoparticles exhibiting peak ORR performance.

Thus we use:

1. Radial distribution functions (RDF);
2. A coordination vector threshold to distinguish surface and bulk atoms;
3. Number of first neighbors (coordination number);

4. Atomic stress and 5-fold index;
5. Analysis of surface arrangement in terms of rhombic structures.

The coordination vector is defined as the sum of all the vectors pointing from first-neighbors to the given atom, and a given Pt atom is defined as a bulk atom if the norm of the coordination vector is smaller than a given threshold (0.6 Å), and as a surface atom otherwise, in analogy with the approach taken in Ref. 16. The Cauchy atomic stress tensors on atom i ($\boldsymbol{\sigma}^i$) used in Fig. 2.12 is defined as Ref. 37:

$$\boldsymbol{\sigma}^i = \frac{1}{\Omega_i} \cdot \{ \frac{1}{2} \sum_j \boldsymbol{F}_{ij} \otimes \boldsymbol{r}_{ij} \}$$

Where Ω_i is the atomic volume of atom i, and the sum is taken over all j-neighbors of i, at a distance $\boldsymbol{r}_{ij}$ each and exerting a force $\boldsymbol{F}_{ij}$ upon i. Given that atomic volumes are not well defined for a deformed solid, we follow common practice of reporting in Fig.3 the products $\boldsymbol{\sigma}^i \cdot \Omega_i$ in units of atm · nm^3. Another useful quantity reported in the main text is the surface energy ($E_{surface}$), defined as:

$$E_{surface} = = \frac{1}{A} \cdot \{ E_{system} - N\, E_{bulk} \}$$

Where A is the surface area, which is the excess energy of the system (E_{system}) with respect to the bulk (E_{bulk}). The 5-fold index is finally defined as the ratio of icosahedral fingerprint [5,5,5] triplets to the total number of triplets in Common Neighbor Analysis.[31-34]

As shown in Figs. 2.12, 2.13 and Table 2.2, the jagged Pt nanowire exhibits structural features that are qualitatively and quantitatively similar to de-alloyed Pt_3Ni_7 nanoparticles,[16] but with an

increase in ORR-favorable patterns, thus explaining our experimentally observed superior ORR catalytic activity for these NW. A configuration from the protocol using Reactive Molecular Dynamics (steps 1-7 above) together with the structure locally relaxed using SMA potential are provided as a further Supplementary Material.

Computational results

The RMD simulation resulted in a pure Pt NW containing 7,165 Pt atoms (in a length of ~ 46 nm) with a diameter of ~ 2.2 nm and highly jagged surface (Fig. 2.12, A and B). Notably, the overall morphology of the predicted J-PtNWs resembles closely the experimentally obtained J-PtNWs as shown in TEM images in Fig. 1, both of which show modulating thread-like segments about 2.2 nm in diameter, containing striction regions, bending points and jagged surfaces.

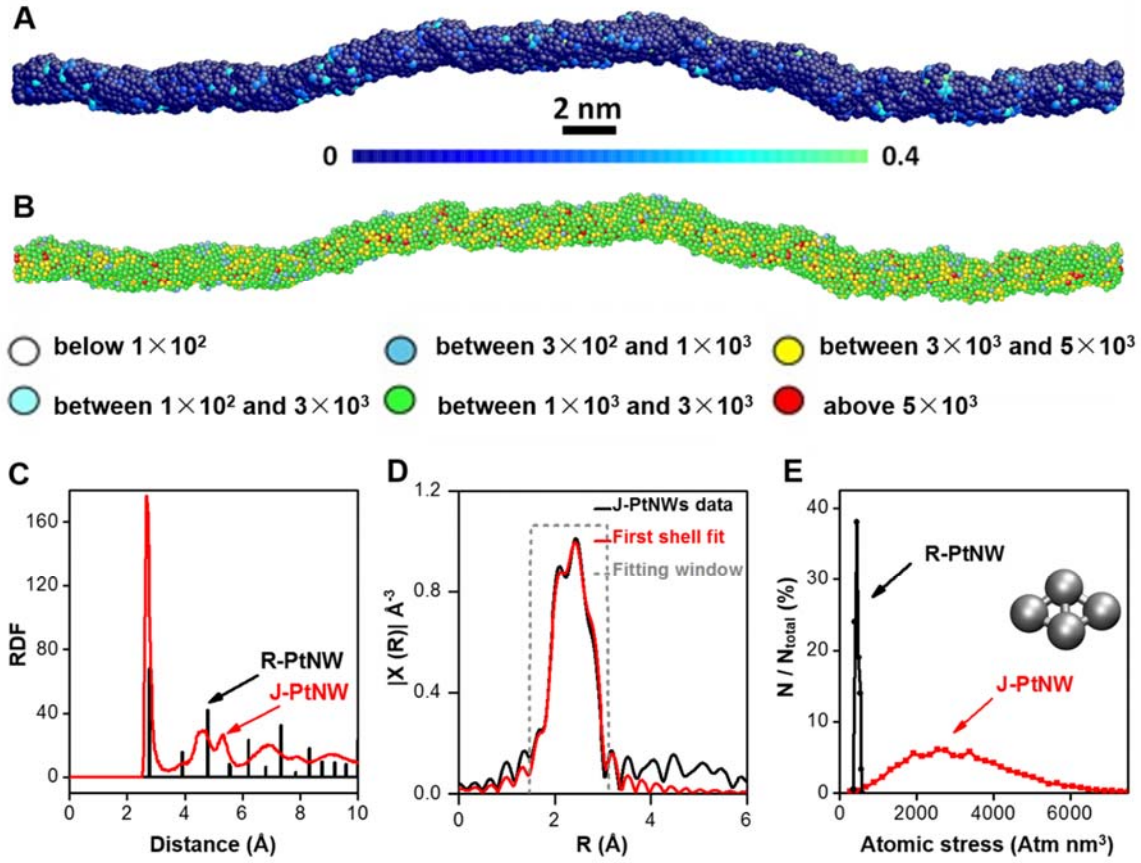

Figure 2.12. Structural analysis of the J-PtNWs obtained from Re axFF reactive molecular dynamics and x-ray absorption spectroscopy. Using the ReaxFF reactive force field we carried out reaction dynamics simulations of the de-alloying process as described in detail in the SI, with an example of the final ReaxFF structure shown in A and B, with an average diameter of ~2.2 nm and length of ~46 nm. (**A**) Each atom of the predicted J-PtNW is colored to show the 5-fold index, i.e., the ratio of icosahedral fingerprint [5,5,5] triplets to the total number of triplets in Common Neighbor Analysis [29, 31, 33]: the lower value of the 5-fold index indicates a less icosahedral-like coordination environment and a better crystallinity, which correlates with the increased activity [16, 29]. (**B**) Each atom of the predicted J-PtNW is colored to show distribution of atomic stress (in atm·nm^3). The magnitudes are distinguished by colors. (**C**) Pt-Pt radial distribution function (RDF)

of the SMA-predicted J-PtNW (red) compared with the peaks of the RDF for the regular PtNW (black). This leads to average Pt-Pt bond distances of 2.70 Å for J-PtNW compared to 2.77 for bulk Pt. (**D**) Pt L_3 edge FT-EXAFS spectrum (black) collected ex situ and the corresponding first shell least-squares fit (red) for the J-PtNWs, revealing that the first shell Pt-Pt bond length in the J-PtNWs (2.71 Å) is ~ 1.8% shorter than that of the Pt foil (2.76 Å), consistent with our calculated distance of 2.70 Å for J-PtNW) and 2.77 for bulk Pt. (**E**) Distribution of the absolute values of the average atomic stress on surface rhombi for the R-PtNWs (black) and the J-PtNWs (red). A rhombus is an ensemble of 4 atoms arranged as two equilateral triangles sharing one edge as shown in the inset.

The predicted radial distribution function (RDF) for the J-PtNW exhibits a well-defined first-neighbor peak at about 2.70 Å (Fig. 2.12 C), which is ~2.2 to 2.5% shorter than the Pt-Pt first-neighbor distance predicted for the R-PtNWs (2.76 Å) and the bulk Pt crystal (2.77 Å), whereas the peaks associated with the second and further neighbors are much broader and more blurred, similar to those reported in nanoporous NPs.[16] These predicted Pt-Pt first-neighbor distance are well confirmed by the EXAFS analysis (Fig. 2.12 D), which reveals that the first shell Pt-Pt bond length in the J-PtNWs (2.71 Å) is ~ 1.8% shorter than that of the Pt foil (2.76 Å). Nanowires with small diameters (~2.2 nm in this case) inherently have ultrahigh surface area that can be further enhanced by the surface roughness of a jagged morphology. We calculated the van der Waals (vdW) surface area of the simulated J-PtNWs to be ~ 110 m^2/g_{Pt} (Table 2.2), which agrees well with our experimental value derived from the ECSA (118 m^2/g_{Pt}).

Table 2.2 Geometric analysis of the final predicted structure of 46-nm-long de-alloyed Pt nanowire (snapshot from the RMD trajectory) compared with the typical predicted structure of a

fully de-alloyed Pt_3Ni_7 NP (initially 10 nm in diameter, finally around 8 nm in diameter) taken from. [16]

	vdW Surface Area (m^2/g_{Pt})	**Surface Atoms N (%)**	**ORR-favorable Rhombi N (%)**
De-alloyed NW	110	49%	76 %
NP (70% Ni)	61	26%	57 %

However, the enhancement of surface area alone cannot fully account for the observed ORR mass activity. Stressed and undercoordinated crystalline-like surface rhombi can dramatically decrease the reaction barrier of the rate determining steps of ORR, thus, improving specific ORR activity.[16] Surface rhombi are an ensemble of 4 atoms arranged as two equilateral triangles sharing one edge (see the inset in Fig. 2.12 E) and resembling the triangular tessellation of an fcc (111) surface, which we find to be superior to a square tessellation for ORR activity in the same way that the fcc (111) surface is more ORR-active than other compact *fcc* surfaces such as fcc (100).[1, 28] Moreover, rhombi that are stressed and under-coordinated but still crystalline-like exhibit smaller overall energy barriers for ORR than those encountered on the rhombi of the fcc (111) surface, as predicted via density-functional theory (DFT) calculations.[16]

Several factors could contribute to the greatly enhanced ORR activity in the J-PtNWs. First, our analysis shows that the coordination number of surface atoms in of the J-PtNWs ranges mostly between 6 and 8 (Fig. 2.13 A), indicating that these surface atoms are under-coordinated when compared to typical crystal surfaces (with coordination numbers of 8 or 9 for (100) or (111) facets, respectively). Despite the low-coordination number and jagged feature, the crystalline-like character of surface atoms in J-PtNWs is confirmed from common neighbor analysis (CNA).[29-31] CNA result shows that the ratio of CNA [5, 5, 5] triplets (a finger print of icosahedral structure) [32]

to the total number of CNA triplets is rather low (84% of the atoms have a ratio below 0.0065) (Fig. 3A). Because the bonded pairs of type [5, 5, 5] are characteristic of icosahedral order, this low [5, 5, 5] ratio indicates a more crystalline-like feature [30] for our established model, which is also a crucial factor for enhancing ORR activity.[16] Indeed, such crystalline-like character of simulation model is consistent with the experimental FFT images (insets in Fig. 2.2 F and 2.2 I) showing that the J-PtNWs remain fcc-like after CV activation and repeated cycling test. Additionally, the distribution of rhombus dihedral angles (Fig. 2.13 B) shows that most of the dihedral angles formed between the two triangles of the rhombus range between 156° and 180°. Comparing with 180° for typical crystalline Pt (111) facet, this statistical analysis further confirms the high-crystallinity nature of the J-PtNWs, which is favorable for increased reactivity.[16] Second, the surface atoms in the J-PtNWs exhibit rather high value of atomic stress about 10 times larger than that for regular (100) or (111) facets (Fig. 2.12, B and E), as also confirmed by simulated and EXAFS derived Pt-Pt distances (Fig. 2.12, C and D). The mechanical strain can decrease the binding energy of adsorbents on close-packed surfaces, which can make the surfaces more active, [30, 34-35] further contributing to the activity enhancement. Finally and importantly, we found that the J-PtNWs possess both a large ECSA (see Table 2.2) and exhibit an unusually high number of the ORR-favorable rhombic structures on the surface. There are 76% rhombi per surface atom in the J-PtNW surface (Table 2.2), considerably higher than 57% previously reported for the nanoporous Pt-NPs. [16]

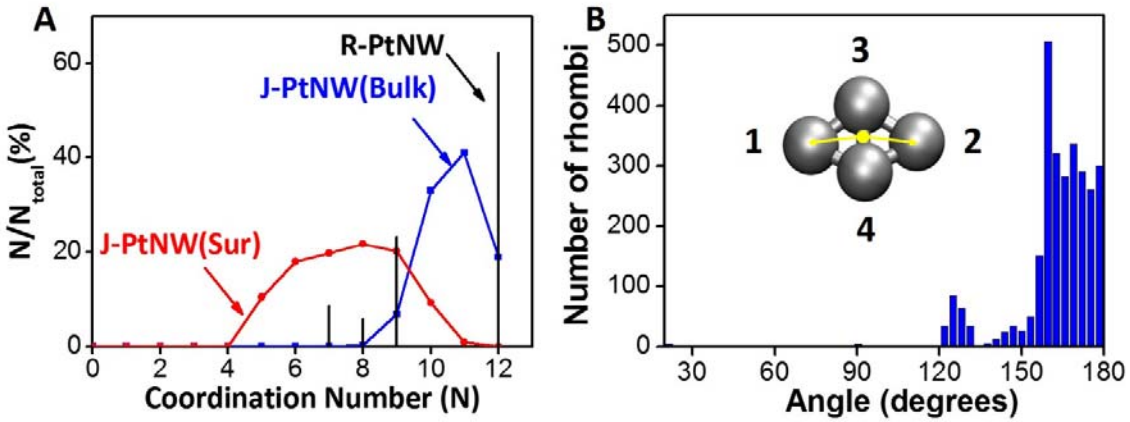

Figure 2.13. (**A**) Coordination number for surface atoms (red) and bulk atoms (blue) of the J-PtNWs, and atoms (black) of R-PtNWs evaluated by counting all neighbors within a distance cut-off of 3.0 Å. (**B**) Schematic depiction of a rhombus (inset) and the distribution of the dihedral angle between the two triangles of the rhombus as defined by the angle formed between the two lines connecting atom 1 and 2 to the middle point of atom 3,4 respectively (highlighted by the yellow arrows in the inset). Most of the angles are between 156° and 180°, which suggest that the surface of the J-PtNWs are highly comparable typical crystalline structure.

2.5 Conclusion

In summary, our experimental studies demonstrate that the formation of ultrafine **J-PtNWs enables an extraordinary ORR activity that nearly doubles the highest Pt mass activity reported to date.** The computational analysis indicates that this exceptional activity arise from surface configurations with richly populated rhombic structures that are crystalline-like but under-coordinated and stressed to reduce the barriers for the rate determining step of ORR, leading to greatly improved specific activity. Additionally, by adopting the 1D NW geometry, the ultrafine J-PtNWs (~2 nm) can exhibit exceptionally high and stable ECSA that has not been achieved in typical NP catalysts. To achieve a high ECSA typically requires NPs as small as possible (e.g., <3

nm). For such small 0D NP, we expect that they have only a "single point contact" with the carbon support, making them rather mobile, so that they tend to move and aggregate, reducing their high surface area and overall activity. In contrast, the J-PtNWs on a carbon support form "multiple-anchor-point line contacts" that firmly lock the NWs in place, ensuring they do not migrate and aggregate during CV cycles. Thus, ultrafine J-PtNWs (~2 nm) can function as stable ORR catalysts to offer an unprecedented ECSA, nearly doubling that of the best reported catalysts to date. Furthermore, the "multi-point line contacts" between the J-PtNWs and carbon support offer a much greater possibility for efficient charge transport and collection, since electrons generated at active surface sites can always be efficiently transported within the metallic NWs, and across PtNW/carbon interface through one of the best electronic contacting point along the "multi-point line contacts" to reach the conductive carbon support and be collected by the electrode. In contrast, the "single point contact" between a nanoparticle catalysts and the carbon support may not always offer an optimal electronic interface for efficient charge transport to the carbon support.

2.6 References

1. V. R. Stamenkovic, B. Fowler, B. S. Mun, G. Wang, P. N. Ross, C. A. Lucas, N. M. Marković, Improved oxygen reduction activity on $Pt_3Ni(111)$ *via* increased surface site availability. *Science* **315**, 493–497 (2007).

2. N. S. Porter, H. Wu, Z. Quan, J. Fang, Shape-control and electrocatalytic activity-enhancement of Pt-based bimetallic nanocrystals. *Acc. Chem. Res*. **46**, 1867–1877 (2013).

3. J. Wu, H. Yang, Platinum-based oxygen reduction electrocatalysts. *Acc. Chem. Res.* **46**, 1848–1857 (2013).

4. Y. J. Wang, N. Zhao, B. Fang, H. Li, X. T. Bi, H. Wang, Carbon-supported Pt-based alloy electrocatalysts for the oxygen reduction reaction in polymer electrolyte membrane fuel cells: particle size, shape, and composition manipulation and their impact to activity. *Chem. Rev.* **115**, 3433–3467 (2015).

5. Z. Peng, H. Yang, Designer platinum nanoparticles: control of shape, composition in alloy, nanostructure and electrocatalytic property. *Nano Today* **4**, 143–164 (2009).

6. D. Wang, H. L. Xin, R. Hovden, H. Wang, Y. Yu, D. A. Muller, F. J. DiSalvo, H. D. Abruña, Structurally ordered intermetallic platinum-cobalt core-shell nanoparticles with enhanced activity and stability as oxygen reduction electrocatalysts. *Nat. Mater.* **12**, 81–87 (2013).

7. C. Wang, M. Chi, G. Wang, D. van der Vliet, D. Li, K. More, H. Wang, J. A. Schlueter, N. M. Markovic, V. R. Stamenkovic, Correlation between surface chemistry and electrocatalytic properties of monodisperse PtxNi1-x nanoparticles. *Adv. Funct. Mater.* **21**, 147–152 (2011).

8. D. F. van der Vliet, C. Wang, D. Tripkovic, D. Strmcnik, X. F. Zhang, M. K. Debe, R. T. Atanasoski, N. M. Markovic, V. R. Stamenkovic, Mesostructured thin films as electrocatalysts with tunable composition and surface morphology. *Nat. Mater.* **11**, 1051–1058 (2012).

9. V. R. Stamenkovic, B. S. Mun, M. Arenz, K. J. J. Mayrhofer, C. A. Lucas, G. Wang, P. N. Ross, N. M. Markovic. Trends in electrocatalysis on extended and nanoscale Pt-bimetallic alloy surface. *Nat. Mater.* **6**, 241–247 (2007).

10. D. F. van der Vliet, C. Wang, D. Li, A. P. Paulikas, J. Greeley, R. B. Rankin, D. Strmcnik, D. Tripkovic, N. M. Markovic, V. R. Stamenkovic, Unique electrochemical adsorption properties of Pt-skin surfaces. *Angew. Chem. Int. Ed.* **51**, 3139–3142 (2012).

11. C. Cui, L. Gan, M. Heggen, S. Rudi, P. Strasser, Compositional segregation in shaped Pt alloy nanoparticles and their structural behavior during electrocatalysis. *Nat. Mater.* **12**, 765–771 (2013).

12. V. R. Stamenkovic, B. S. Mun, K. J. J. Mayrhofer, P. N. Ross, N. M. Marković, Effect of Surface Composition on Electronic Structure, Stability, and Electrocatalytic Properties of Pt-Transition Metal Alloys: Pt-Skin versus Pt-Skeleton Surfaces. *J. Am. Chem. Soc*. **128**, 8813–8819 (2006).

13. F. Calle-Vallejo, J. I. Martínez, J. M. García, Lastra, P. Sautet, D. Loffreda, Fast prediction of adsorption properties for platinum nanocatalysts with generalized coordination numbers. *Angew. Chem. Int. Ed.* **53**, 8316–8319 (2014).

14. F. Calle-Vallejo, J. Tymoczko, V. Colic, Q. H. Vu, M. D. Pohl, K. Morgenstern, D. Loffreda, P. Sautet, W. Schuhmann, A. S. Bandarenka, Finding optimal surface sites on heterogeneous catalysts by counting nearest neighbors. *Science* **350**, 185–189 (2015).

15. M. E. Escribano, P. Malacrida, M. H. Hansen, U. G. V. Hansen, A. V. Palenzuela, V. Tripkovic, J. Schiøtz, J. Rossmeisl, I. E. L. Stephens, I. Chorkendorff, Tuning the activity of Pt alloy electrocatalysts by means of the lanthanide contraction. *Science* **352**, 73–76 (2016).

16. A. Fortunelli, W. A. Gorddard III, L. Sementa, G. Barcaro, F. R. Negreiros, A. J. Botero, The atomistic origin of the extraordinary oxygen reduction activity of Pt_3Ni_7 fuel cell catalysts. *Chem. Sci.* **6**, 3915–3925 (2015).

17. S. Choi, S. Xie, M. Shao. J. H. Odell, N. Lu, H. C. Peng, L. Protsailo, S. Guerrero. J. Park, X. Xia, J. Wang, M. J. Kim, Y. Xia, Synthesis and characterization of 9 nm Pt-Ni octahedral with

a record high activity of 3.3A/mg$_{Pt}$ for the oxygen reduction reaction. *Nano Lett.* **13**, 3420–3425 (2013).

18. X. Huang, Z. Zhao, Y. Chen, E. Zhu, M. Li, X. Duan, Y. Huang, A rational design of carbon-supported dispersive Pt-based octahedral as efficient oxygen reduction reaction catalysts. *Energy Environ Sci.* **7**, 2957-2962 (2014).

19. X. Huang, Z. Zhao, L. Cao, Y. Chen, E. Zhu, Z. Lin, M. Li, A. Yan, A. Zettl, Y. M. Wang, X. Duan, T. Mueller, Y. Huang, High-performance transition metal-doped Pt_3Ni octahedral for oxygen reduction reaction. *Science* **348**, 1230–1234 (2015).

20. H. Zhu, S. Zhang, S. Guo, D. Su, S. Sun, Synthetic control of FePtM nanorods (M = Cu, Ni) to enhance the oxygen reduction reaction. *J. Am. Chem. Soc.* **135**, 7130–7133 (2013).

21. S. Guo, D. Li, H. Zhu, S. Zhang, N. M. Markovic, V. R. Stamenkovic, S. Sun, FePt and CoPt nanowires as efficient catalysts for the oxygen reduction reaction. *Angew. Chem. Int. Ed.* **52**, 3465–3468 (2013).

22. L. Zhang, L. T. Roling, X. Wang, M. Vara, M. Chi, J. Liu, S. Choi, J. Park, J. A. Herron, Z. Xie, M. Mavrikakis, Y. Xia, Platinum-based nanocages with subnanometer-thick walls and well-defined, controllable facets. *Science* **24**, 412–416 (2015).

23. C. Chen, Y. Kang, Z, Huo, Z. Zhu, W. Huang, H. L. Xin, J. D. Snyder, D. Li, J. A. Herron, M. Maverikakis, M. Chi, K. L. More, Y. Li, N. M. Markovic, G. A. Somorjai P. Yang, V. R. Stamenkovic, Highly crystalline multimetallic nanoframes with three-dimensional electrocatalytic surface. *Science* **343**, 1339–1343 (2014).

24. S. Zhang, Y. Hao, D. Su, V. V. T. Doan-Nguyen, Y. Wu, J. Li, S. Sun, C. B. Murray, Monodisperse core/Shell Ni/FePt nanoparticles and their conversion to Ni/Pt to catalyze oxygen reduction, *J. Am. Chem. Soc.* **136**, 15921–15924, (2014).

25. L. Tang, B. Han, K. Persson, C. Friesen, T. He, K. Sieradzki, G. Ceder, Electrochemical stability of nanometer-scale Pt particles in acidic environments, *J. Am. Chem. Soc.* **132**, 596-600, (2010).

26. L. Tang, X. Li, R. C. Cammarata, C. Friesen, K. Sieradzki, Electrochemical stability of elemental metal nanoparticles, *J. Am. Chem. Soc.* **132**, 11722-11726, (2010).

27. C. F. Sanz-Navarro, P. O. Astrand, D. Chen, M. Ronning, A. C. T. van Duin, T. Jacob and W. A. Goddard, Molecular Dynamics Simulations of the Interactions between Platinum Clusters and Carbon Platelets, *J. Phys. Chem. A*, **112**, 1392 – 1402 (2008).

28. Y. Sha, T. H. Yu, B. V. Merinov, P. Shirvanian, W. A. Goddard III, Oxygen hydration mechanism for the oxygen reduction reaction at Pt and Pd fuel cell catalysts. *J. Phys. Chem. Lett.* **2**, 572–576 (2011**)**.

29. D. Faken, H. Jonsson, Systematic analysis of local atomic structure combined with 3D computer graphics. *Comput. Mater. Sci.* **2**, 279–286 (1994).

30. S. Schnur, A. Groß, Strain and coordination effects in the adsorption properties of early transition metals: A density-functional theory study, *Phys. Rev. B*. **81**,033402 (2010).

31. J. D. Honeycutt, H. C. Andersen. Molecular dynamics study of melting and freezing of small Lennard-Jones clusters. *J. Phys. Chem.* **91**, 4950-4963 (1987).

32. F. Cleri, V. Rosato, Tight-binding potentials for transition metals and alloys, *Phys. Rev. B.* **48**, 22-33, (1993).

33. A. Stukowski, Structure identification methods for atomistic simulations of crystalline materials. *Model. Simul. Mater. Sci. Eng.* **20**, 045021 (2012).

34. M. F.Francis, & W. A. Curtin, Mechanical work makes important contributions to surface chemistry at steps. *Nat. Commun*. **6**, 6261 (2015).

35. S. Zhang, X. Zhang, G. Jiang, H. Zhu, S. Guo, D. Su, G. Lu, S. Sun, Tuning Nanoparticle Structure and Surface Strain for Catalysis Optimization, *J. Am. Chem. Soc.* **136**, 7734−7739, (2014).

Chapter 3. Jagged Pt/Ni(OH)$_2$ hybrid nanowires as bifunctional alkaline water electro-catalysts

3.1 Introduction

Hydrogen (H_2), as the energy carrier for proton exchange membrane fuel cell, has been proved to be an exceptional candidate for green energy generation.[1-4] In order to effectively harvest H_2, alkaline water electrolysis is attracting more and more attention due to its advantages such as high purity, accessible set up etc.[5-7] platinum (Pt) is universally recognized as the most efficient element for catalyzing HER especially in acidic media.[8-10] However, the relatively sluggish kinetics of HO–H bond cleavage limits the catalytic performance of Pt in alkaline condition[11-13], which is the major limitation for realistic alkaline water system.

Previous studies have shown that combing Pt-based material with transition metal hydroxide species could greatly improve the catalytic kinetics for HER in alkaline electrolyte[14,15]. However, the overall mass activity achieved to date remains relatively low[12,13], which could seriously limit practical applications due to the high cost of Pt. Thus, improving the Pt mass activity for HER is essential for cost effective electrolysis and hydrogen production. Inspired by our previous development of ultrafine jagged Pt nanowires (J-PtNWs) as highly efficient oxygen reduction reaction (ORR) catalyst[16], we further explore the surface decoration of J-PtNWs to produce a unique J-PtNW/Ni(OH)$_2$ hybrid catalysts with tailored activity. The resulting J-PtNWs and J-PtNWs/Ni(OH)$_2$ could exhibit a record high mass activity of 6.9 and 11.8 A/mg$_{Pt}$ for HER at -70 mV vs. RHE and pH 14, which are 9.8 and 17 times higher than that of commercial Pt/C. Density functional theory calculations reveal rich hot-spots on models of both J-PtNWs and of J-PtNWs/Ni(OH)$_2$, positively impacting the alkaline HER kinetics. Moreover, we further show that such surface modification could also greatly enhance the OER activity, thus creating a superior

bifunctional electro-catalysts for both HER and OER, and enable a water splitting mass activity of 0.6 A/mg_{Pt} at 1.6 V *vs.* RHE.

3.2 Material synthesis and characterizations

Pt-Ni nanowire synthesis

A simple one-pot synthetic procedure followed by an annealing process was used to produce the Pt-Ni NWs with an average length of 300 nm and diameter of 4.5 nm (Fig 3.1 A). In a typical synthesis, 20 mg $Pt(acac)_2$ and 40 mg $Ni(acac)_2$ were mixed with 130 mg glucose, 1.7 mg $W(CO)_6$ and 60 mg PVP 40 in a glass vial. 5 ml of oleylamine and octadecene (3:2 volume ratio) was used as co-solvent. The mixture was heated to 140 ºC for 6 hours to form Pt-NiO core-shell nanowires. The result nanowires were collected via centrifuge at 7000 rpm for 20 min. After loading the nanowires on carbon black, the catalyst were than annealed under 450 ºC in argon/hydrogen (97:3) atmosphere for 12 hours to get the PtNi alloy nanowires/carbon. The resulted Pt-Ni NWs were dispersed on carbon support in ethanol to form the catalyst ink, which was then casted on glassy carbon rotating disk (RDE, geometry area = 0.196 cm^2) electrode to form a homogeneous film.

J-PtNWs and J-PtNWs/$Ni(OH)_2$ preparation

An electrochemical de-alloying process was performed via cyclic voltammetry (CV) between 0.05 V - 1.1 V vs. RHE in 0.1 M $HClO_4$ to obtain jagged platinum nanowires (J-PtNWs). The ECSA (determined by H_{upd} at 0.05 V – 0.35 V vs. RHE) gradually increases with increasing CV cycles and eventually stabilizes at about 120 m^2/g_{Pt} after 150-200 CV cycles, which indicates the completion of de-alloying step. The average diameter is reduced from 4.5 nm before to 2.2 nm

after the de-alloying process (Fig 3.1 B). The resulted J-PtNWs feature a rough surface and an ultrahigh ECSA of 120 m^2/g_{Pt}, greatly exceeding that of commercial Pt/C materials or most advanced Pt nanostructure electrocatalysts (50-70 m^2/g_{Pt}). To obtain J-PtNWs/$Ni(OH)_2$, we stop the acidic CV at the 140th cycle to preserve a small portion of Ni atoms near the surface of NWs.

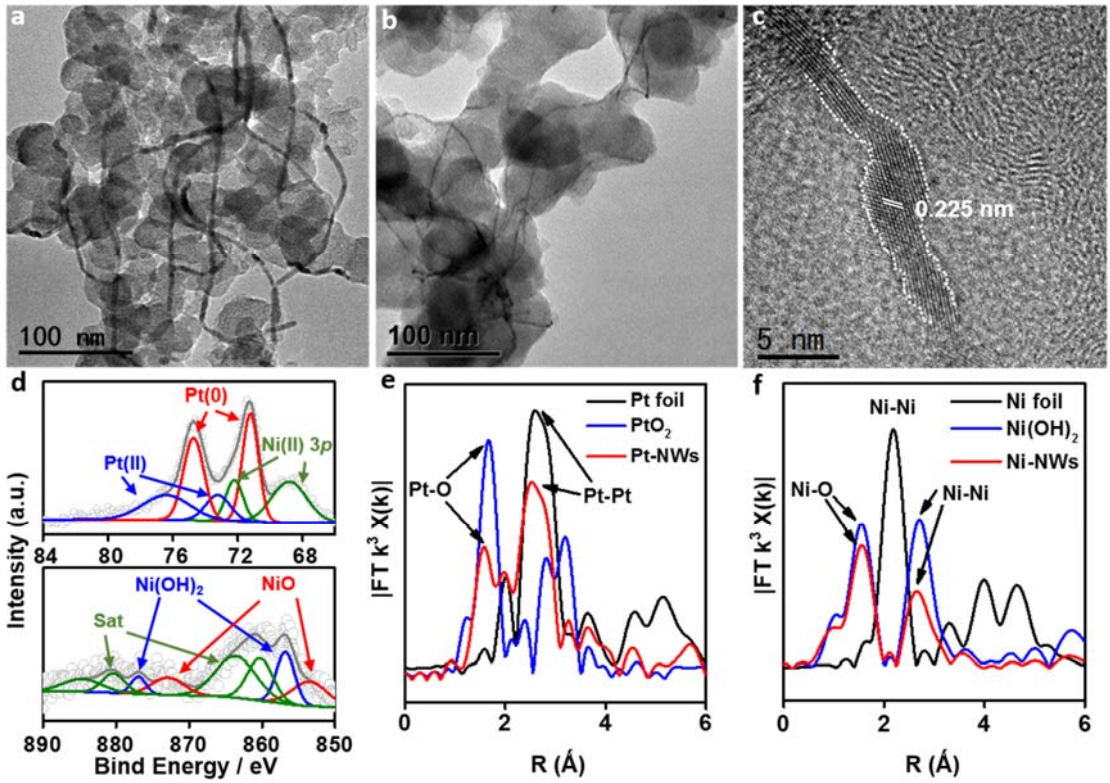

Figure 3.1. Characterization results for as-obtained Pt-Ni NWs and J-PtNWs/$Ni(OH)_2$. TEM image of (**A**) Pt-Ni alloy nanowires and (**B**) J-PtNWs/$Ni(OH)_2$. (**C**) HRTEM image of J-PtNWs/$Ni(OH)_2$. (**D**) Pt and Ni XPS of J-PtNWs/$Ni(OH)_2$. (**E**) Pt EXAFS fitting result and (**F**) Ni EXAFS fitting result of J-PtNWs/$Ni(OH)_2$.

Next step, the RDE is rinsed in 1 M KOH, and cycled between 0.05 V – 1.6 V in nitrogen-saturated 1 M KOH for another 100 cycles. Comparing with the CVs of other materials such as Pt/C and fully dealloyed J-PtNWs, two exclusive Ni^{2+}/Ni^{3+} redox peaks are apparent in J-

PtNWs/$Ni(OH)_2$ at 1.34 V (Ni^{3+} to Ni^{2+}) and 1.40 V (Ni^{2+} to Ni^{3+}) vs. RHE respectively (see Fig 3.2 A). These typical redox peaks were widely recognized as the evidence of nickel hydroxide species[17]. High-resolution transmission electron microscopy (HRTEM) shows that the (111) spacing of J-PtNWs/$Ni(OH)_2$ is 0.225 nm (Fig. 3.1 C), which is about 2.2 % smaller compare with that of crystalline platinum (0.230 nm).

Material characterizations

High-angle annular dark-field scanning transmission electron microscope (HAADF-STEM) shows a well-maintained ultrafine one-dimensional (1D) crystalline configuration (Fig 3.2). The overall composition of J-PtNWs/$Ni(OH)_2$ was determined by energy-dispersive x-ray (EDX) spectroscopy elemental mapping (Fig 3.2) and inductively coupled plasma (ICP) atomic emission spectrometry analysis. The result shows a Pt:Ni ratio of 92:8 in J-PtNWs/$Ni(OH)_2$. X-ray photoelectron spectroscopy (XPS) shows a pair of Ni 3p peaks near in Pt 4f region (Fig. 3.1 D), which is consistent with the Ni^{2+} species in $Ni(OH)_2$. Additionally, the Ni 2p XPS spectra shows that the majority chemical state of Ni in J-PtNWs/$Ni(OH)_2$ is Ni^{2+}, confirming that the most Ni-related species are in form of $Ni(OH)_2$ instead of alloyed Ni.

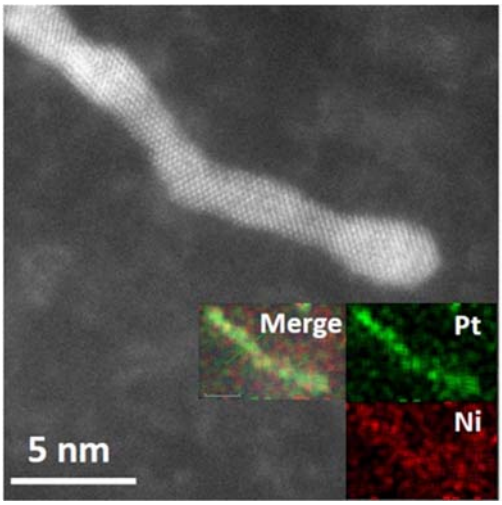

Figure 3.2. HAADF-STEM of J-PtNWs/$Ni(OH)_2$, inset: EDX mapping of the same area shown in figure.

X-ray absorption data analysis

We have also performed X-ray absorption fine structure measurements to probe the local atomistic and electronic structures of the J-PtNWs/$Ni(OH)_2$ sample. The X-ray absorption find structure spectra (Pt L_3-edge and Ni K-edge) were collected at 1W1B station in Beijing Synchrotron Radiation Facility (BSRF). The storage rings of BSRF was operated at 2.5 GeV with a maximum current of 250 mA. Using Si(111) double-crystal monochromator, the data collection was carried out in fluorescence excitation mode using a Lytle detector for PtNi sample, and in transmission mode using a ionization chamber for Pt foil, PtO_2 bulk, Ni foil and $Ni(OH)_2$ bulk All spectra were collected in ambient conditions.

The acquired EXAFS data were processed according to the standard procedures using the ATHENA module implemented in the IFEFFIT software packages. The k^3-weighted EXAFS

spectra were obtained by subtracting the post-edge background from the overall absorption and then normalizing with respect to the edge-jump step. Subsequently, k^3-weighted $\chi(k)$ data of Fe K-edge were Fourier transformed to real (R) space using a hanning windows (dk=1.0 $Å^{-1}$) to separate the EXAFS contributions from different coordination shells. To obtain the quantitative structural parameters around central atoms, least-squares curve parameter fitting was performed using the ARTEMIS module of IFEFFIT software packages.

The following EXAFS equation was used:

$$\chi(k) = \sum_j \frac{N_j S_o^2 F_j(k)}{k R_j^2} \exp[-2k^2\sigma_j^2] \exp[\frac{-2R_j}{\lambda(k)}] \sin[2k R_j + \phi_j(k)]$$

S_0^2 is the amplitude reduction factor, $F_j(k)$ is the effective curved-wave backscattering amplitude, N_j is the number of neighbors in the j^{th} atomic shell, R_j is the distance between the X-ray absorbing central atom and the atoms in the j^{th} atomic shell (backscatterer), λ is the mean free path in Å, $\phi_j(k)$ is the phase shift (including the phase shift for each shell and the total central atom phase shift), σ_j is the Debye-Waller parameter of the j^{th} atomic shell (variation of distances around the average R_j). The functions $F_j(k)$, λ and $\phi_j(k)$ were calculated with the ab initio code FEFF8.2.

The oxidation state of Pt can be probed through the white line intensity at Pt L_3-edge[18,19]. It was found in Pt XANES result (Fig 3.3A) that the white line intensity of our sample was between that of Pt foil and PtO_2, indicating that the average oxidation state of Pt in the J-PtNWs/$Ni(OH)_2$ sample was between zero and four, and a part of Pt species might be oxidized.

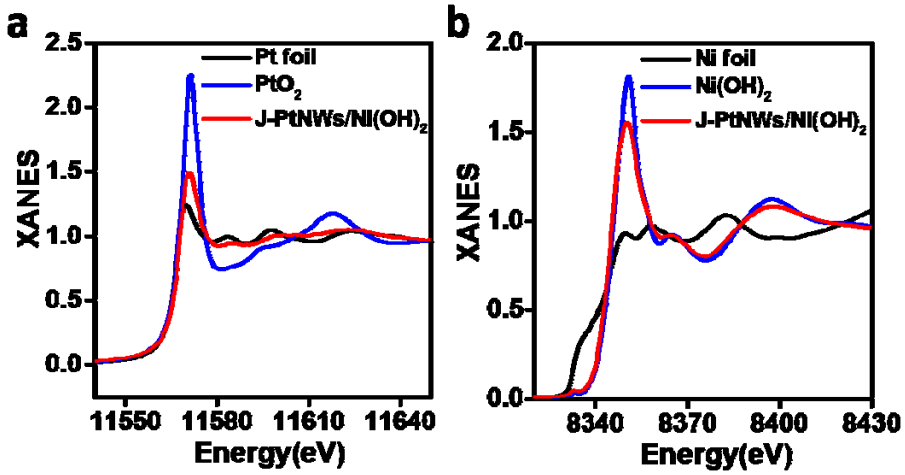

Figure 3.3. (**A**) XANES spectra of Pt L_3-edge and (**B**) XANES spectra of Ni K-edge.

The FT-EXAFS spectra (Fig 3.4) show a main peak at about 2.7 Å with a 2.5% decrease of Pt-Pt bond length when compared with bulk Pt, which is consistent with our previous report[16] and the TEM studies described above.

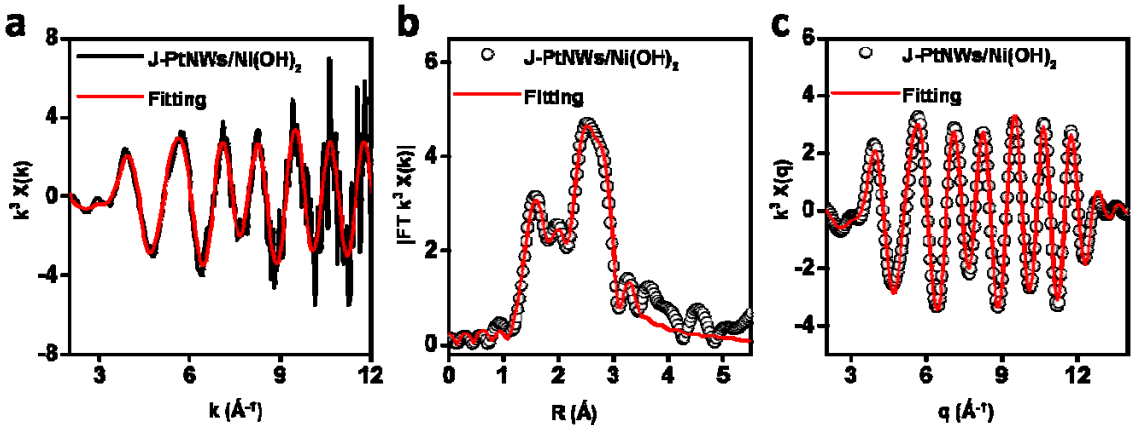

Figure 3.4. Fitting results of J-PtNWs/Ni(OH)$_2$ at Pt L_3-edge. (**A**) The k space fitting curves of (**B**) The FT-EXAFS fitting curves. (FT range: 2-12.5 $Å^{-1}$; fitting range: 0.8-3.4 Å). (**C**) The inversed FT-EXAFS fitting curves.

The Ni K-edge XANES spectra (Fig 3.3 B) of J-PtNWs/$Ni(OH)_2$, Ni foil and $Ni(OH)_2$ bulk show that J-PtNWs/$Ni(OH)_2$ show rather similar features to that of bulk $Ni(OH)_2$ counterpart. The XANES region of Ni K-edge provide information on the oxidation state of Ni species based on the absorption threshold position and white line intensity (due to the allowed 1s→4p transition)[20]. Although the absorption threshold position of J-PtNWs/$Ni(OH)_2$ is really close to that of $Ni(OH)_2$ bulk, its white line intensity is lower than that of $Ni(OH)_2$, suggesting the average oxidation state of Ni in J-PtNWs/$Ni(OH)_2$ is slightly below two.

Both the FT-EXAFS curves (Fig 3.5) of J-PtNWs/$Ni(OH)_2$ and bulk $Ni(OH)_2$ (Fig 3.6)show two obvious peaks at 1.6 Å and 2.7 Å (Fig 3.1 F), which can be attributed to the 1st shell Ni-O and 2nd shell Ni-Ni coordination, respectively. No metallic Ni-Ni or Ni-Pt feature was found in the EXAFS spectrum of the J-PtNWs/$Ni(OH)_2$ sample, demonstrating that the Ni species in our nanowires samples exist as nickel hydroxide state. Interestingly, the Ni-Ni coordination peak of J-PtNWs/$Ni(OH)_2$ is much weaker compared to the Ni-O peak, which may be attributed to the rather low surface coverage and the lack of longer range Ni-Ni ordering in the J-PtNWs sample[21,22], and suggests single or few-atom $Ni(OH)_2$ species on J-PtNW surface.

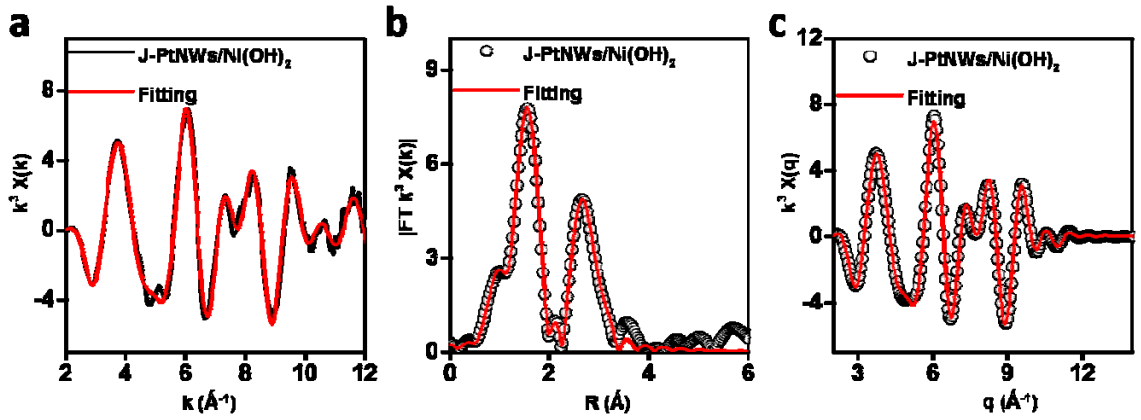

Figure 3.5. Fitting results of J-PtNWs/Ni(OH)$_2$ at Ni k-edge. (**A**) The k space fitting curves of (**B**) The FT-EXAFS fitting curves. (FT range: 2-12.5 Å^{-1}; fitting range: 0.8-3.4 Å). (**C**) The inversed FT-EXAFS fitting curves.

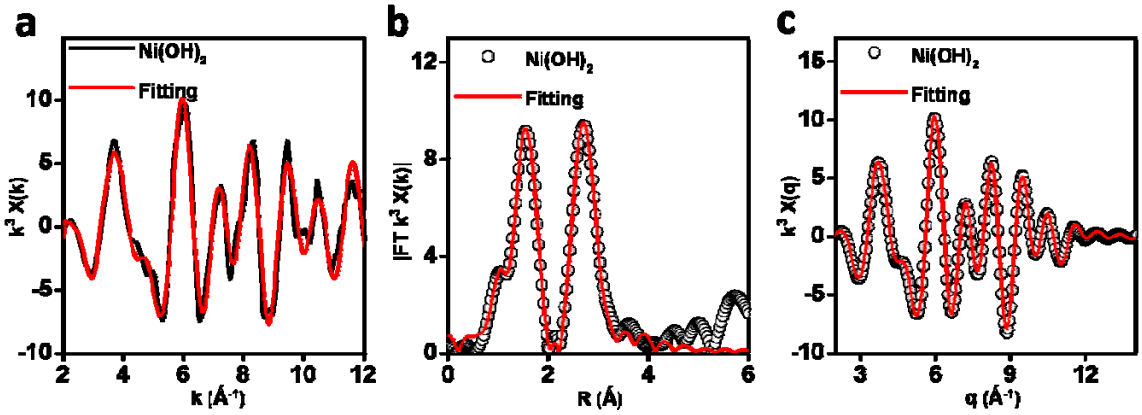

Figure 3.6. Fitting results of Ni(OH)$_2$ at Ni k-edge. (**A**) The k space fitting curves of (**B**) The FT-EXAFS fitting curves. (FT range: 2-12.5 Å^{-1}; fitting range: 0.8-3.4 Å). (**C**) The inversed FT-EXAFS fitting curves.

3.3 Electro-catalysis evaluations

Hydrogen evolution reaction

We have evaluated the HER activity of the J-PtNWs/$Ni(OH)_2$ and compared against J-PtNWs and with commercial Pt/C (10 wt%) using the rotation disk electrode (RDE) test. Alkaline/mercury oxide electrode was used as reference electrode, and graphite rod was used as counter electrode. The reference electrode calibration was completed in H_2-saturated 1 M KOH at room temperature. 1600 rpm rotation speed was applied on working RDE to get rid of generated bubble during the performance test. The specific and mass current density were normalized by the geometry area of RDE and total Pt loading.

The Pt loading on RDE for Pt/C, J-PtNWs, and J-PtNWs/$Ni(OH)_2$ was 3.0 μg/cm^2, 2.0 μg/cm^2, and 2.0 μg/cm^2 respectively. The CV studies of the J-PtNWs/$Ni(OH)_2$ show two exclusive Ni^{2+}/Ni^{3+} redox peaks, which are absent in the Pt/C and J-PtNWs (Fig 3.7 A), which demonstrate the nickel hydroxide species was successfully decorated on de-alloyed nanowires. The HER performance was further evaluated using linear sweep voltammetry (LSV) under room temperature in 1 M N_2-saturated KOH with a scan rate of 5 mV/s. Figure. 3.7 B shows the electrode geometry area normalized LSVs for all samples. The specific activity of all samples can be derived to be **1.8 mA/cm^2**, **13.8 mA/cm^2, and 23.6 mA/cm^2** at -70 mV vs. RHE for Pt/C, J-PtNWs, and J-PtNWs/$Ni(OH)_2$ respectively. Meanwhile at the same potential comparison point, the mass activity derived from Pt loading mass normalized LSV curves (Fig. 3.7 C) shows **0.7 A/mg_{Pt}**, **6.9 A/mg_{Pt}, and 11.8A/mg_{Pt}** for Pt/C, J-PtNWs, and J-PtNWs/$Ni(OH)_2$. The HER mass activities at -70 mV for the two NWs were 9.9, and 16.9 times that of the benchmark Pt/C catalysts. From specific-normalized Tafel diagram of all tested catalysts (Fig. 3.7 D), the J-PtNWs and J-PtNWs/$Ni(OH)_2$ have a Tafel-slop of 41.3 mV/dec and 34.1 mV/dec respectively, far less than the 64.3mV/dec

value of Pt/C, suggesting a much improved HER kinetics occurred on both nanowire catalysts. When we compare the mass-normalized Tafel slopes (Fig. 3.7 E), the 39.3 mV/dec and 33.0 mV/dec values show an even more significant advantage when compared with Pt/C (89.3 mV/dec), which demonstrates a ultra-high platinum- utilisation efficiency for both nanowires when carrying out HER. For such a promoted catalytic behavior of J-PtNWs, our hypothesis is that the defective surface sites could change the binding energy for H species and serve as highly active catalytic hot-spots. Together with the large ECSA nature of the ultrafine 1D NWs, the J-PtNWs/$Ni(OH)_2$ deliver a much higher HER mass activity not previously possible. From the activity comparison chart (Fig. 3.7 F), we can see that after $Ni(OH)_2$ decoration, the resulting J-PtNWs/$Ni(OH)_2$ shows a 1.7 times higher HER activity when compared with J-PtNWs. **Even compared with recently reported state-of-the-art HER catalysts[17,23], our J-PtNWs/$Ni(OH)_2$ exhibit more than 9 times higher mass activity than the previous record HER catalyst (Table 3.1)**.

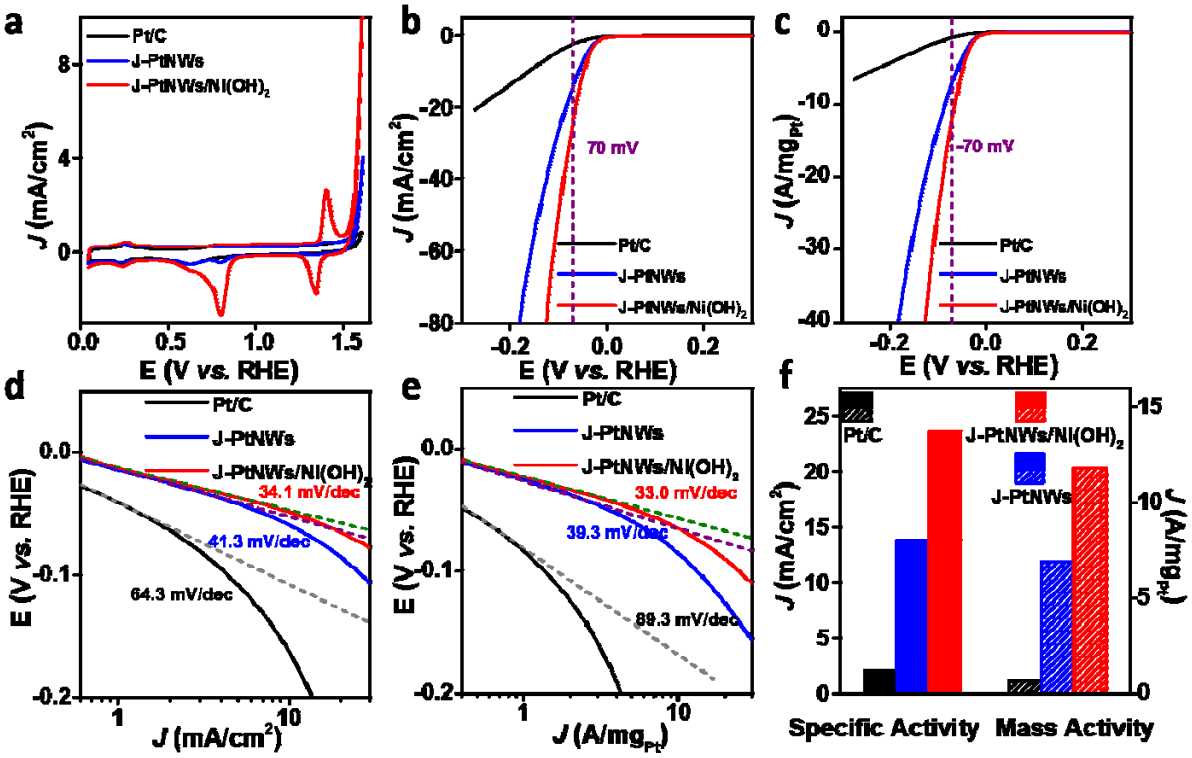

Figure 3.7. Electrocatalytic results for Pt/C, J-PtNWs, and J-PtNWs/Ni(OH)$_2$, 1M KOH was used as the electrolyte in all tests. (**A**) Cyclic voltammetry (CV) diagram performed between 0.05 V – 1.6 V vs. RHE with a scan rate of 50 mV/s. (**B**) RDE surface area (0.196 cm^2) normalized and (**C**) Pt mass loading normalized HER LSVs, the scan rate was 5 mV/s with 95% *i*R-compensation. (**D**) Specific area and (**E**) Pt mass normalized HER Tafel-slope. (**F**) Specific and mass activities comparison for HER at -70 mV.

Oxygen evolution reaction

The CV plot in Fig. 2a also suggests prominent catalytic activity of J-PTNWs/Ni(OH)$_2$ catalysts for oxygen evolution reaction (OER), the other half reaction of water splitting process. Notably, near the OER region around 1.5 V vs. RHE, the J-PtNWs/Ni(OH)$_2$ sample showed

considerably higher current than that of Pt/C or J-PtNWs, suggesting an exceptional OER activity. A close examination of OER activity using LSV (Fig 3.8 A) can clearly reveal the impact brought by defective sites on Pt surface and the existence of $Ni(OH)_2$ species. Initially, the OER on-site potential of Pt/C was 1.702 V. When defective sites concentrated catalytic surface on J-PtNWs, the on-site potential was lowered to 1.547 V. Finally, with additional $Ni(OH)_2$ decoration, the on-site potential was further decrease to 1.487 V. The corresponding mass-normalized Tafel diagram also shows a similar trend as the HER side. Both J-PtNWs (54.2 mV/dec) and J-PtNWs/$Ni(OH)_2$ (35.2 mV/dec) exhibit a much lower slope when compared with Pt/C (188.6 mV/dec) at pH 14 (Fig. 3.8 B), which indicated a significantly improved OER kinetics occurred on both of our Pt-based nanowire materials.

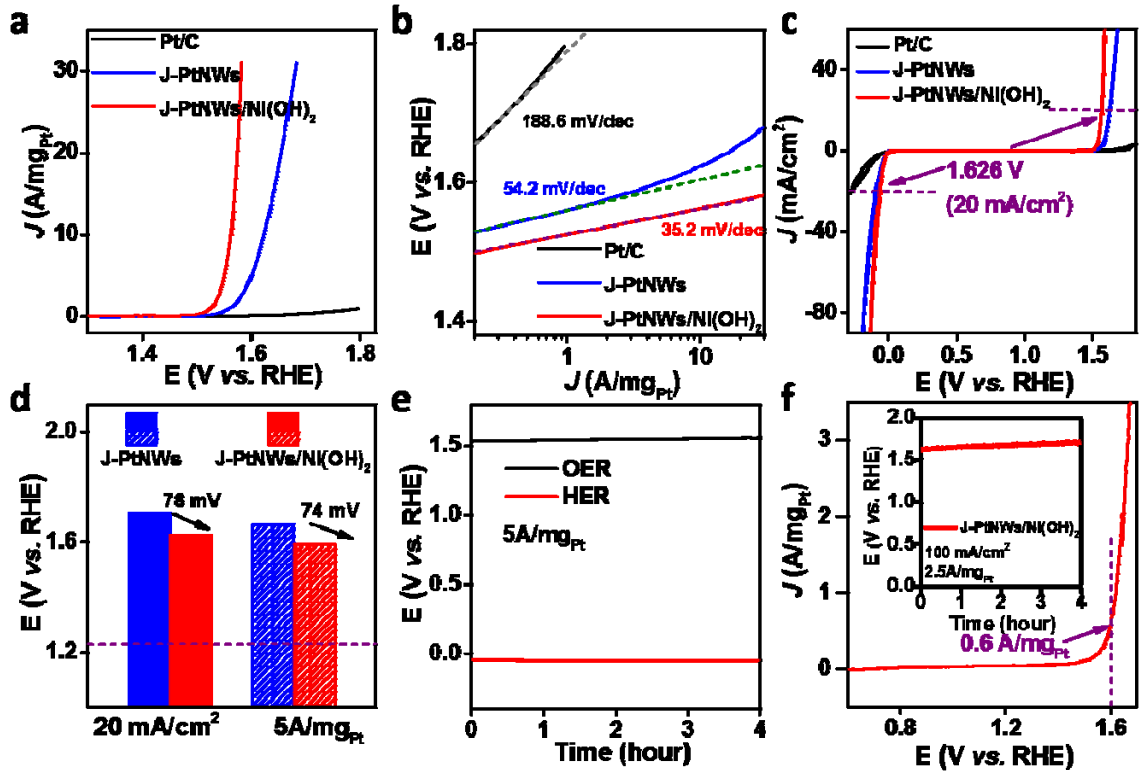

Figure 3.8. OER and water splitting electrocatalytic results, 1M KOH was used as the electrolyte in all tests. (**A**) The OER LSVs Chronopotentiometry of J-PtNWs/$Ni(OH)_2$ under

current density of 5A/mg_{Pt} for both HER and OER. (**B**) The water splitting over-potential comparison of R-PtNWs, J-PtNWs, and J-PtNWs/$Ni(OH)_2$ respectively when reached 20 mA/cm^2 and 5A/mg_{Pt}. (**C**) OER and HER tafel slop of J-PtNWs/$Ni(OH)_2$. (**D**) The two electrode water splitting polarize curve of J-PtNWs/$Ni(OH)_2$ on carbon paper. The scan rate was 5 mV/s with 95% *i*R-compensation. The inset figure shows chronopotentiometry of J-PtNWs/$Ni(OH)_2$ on carbon paper under current density of 100 mA/cm^2, the current density was normalized by electrode geometry surface area, the Pt mass loading was 35 $\mu g/cm^2$.

Table 3.1 HER activity and water splitting over-potential comparison of J-PtNWs/$Ni(OH)_2$, J-PtNWs, R-PtNWs, and Pt/C catalysts.

	HER in 1M KOH @ -0.07 V		**Over-potential of water splitting (mV)**	
	Specific activity (mA/cm^2)	Mass Activity (A/mg_{Pt})	20 mA/cm^2	5 A/mg_{Pt}
Pt/C (this work)	1.8	0.7	NA	NA
J-PtNWs	**13.8**	**6.9**	**474**	**435**
J-PtNWs/$Ni(OH)_2$	**23.6**	**11.8**	**396**	**361**

PtNWs/SL $Ni(OH)_2$[17]	NA	0.679	NA	NA
Pt3Ni2 NWs-S/C[23]	19.1	1.25	NA	NA

To further demonstrate the water splitting property of our materials, we conduct a cyclic voltammetry (CV) test on RDE system to monitor both the HER and OER catalytic performance. As shown in Fig 3.8 C, the J-PtNWs/$Ni(OH)_2$ shows an obvious advantage over either J-PtNWs or Pt/C, and needs only 1.632V overall potential for both HER and OER to reach a specific activity of 20 mA/cm^2. When we compare the over potential when HER and OER simultaneously achieve a specific activity of 20 mA/cm^2 or mass activity of 5A/mg_{Pt} (Fig 3.8 D), the $Ni(OH)_2$ decorated J-PtNWs lower the over-potential to reach the specific and mass activity targets by 78 mV and 74 mV respectively compared to bare J-PtNWs. HER and OER chronopotentiometry tests were performed in 1 M KOH at room temperature to evaluate the durability of J-PtNWs/$Ni(OH)_2$. A constant current density of 5 A/mg_{Pt} was applied for 4 hours. The working electrode was first set to perform 4-hour OER stability test, afterwards the same electrode was used to carry out the HER stability test. As shown in Fig 3.8 E, after 4 hours stability test on each side of water splitting reaction, the overall potential when both HER and OER reach 5 A/mg_{Pt} shows negligible change, indicating that the decorated $Ni(OH)_2$ species are stable on the defective surface of J-PtNWs during the durability test. The TEM images of the J-PtNWs/$Ni(OH)_2$ largely retained its initial NW morphology after the stability test, thus maintaining their stability. In contrast, the Pt/C shows significant aggregation (Fig 3.9), consistent with rapid degrading catalytic performance.

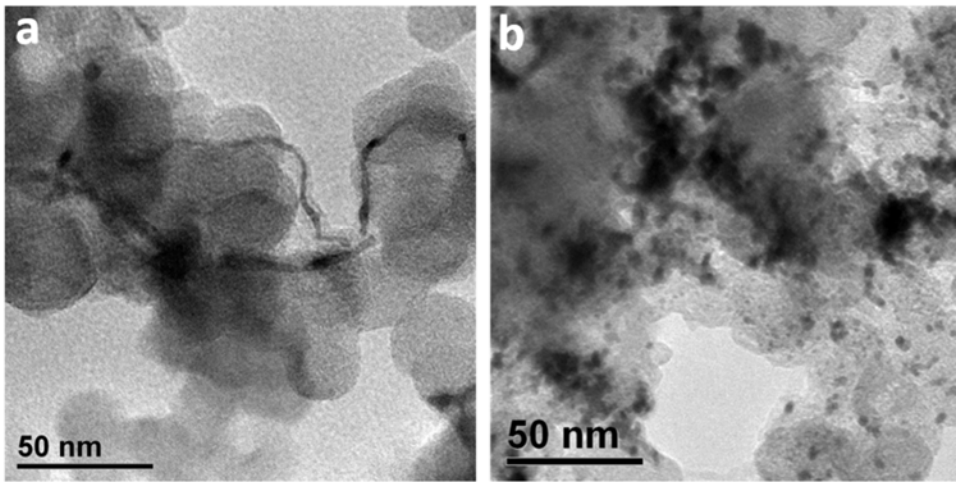

Figure 3.9. TEM images of (**A**) J-PtNWs/$Ni(OH)_2$ and (**B**) Pt/C after stability test.

To approach practical water electrolysis condition, we have cast J-PtNWs/$Ni(OH)_2$ onto carbon paper with Pt loading of 20 μg/cm^2. The chronopotentiometry test shows a similar stability with an order of magnitude higher loading (Fig. 3.8 F inset). Importantly, the two electrode linear scan voltammetry result exhibit a water splitting on-site potential of 1.488 V, and an extraordinary mass activity of 0.6 A/mg_{Pt} at 1.6 V (Fig. 3.8 F).

3.4 The origin of HER activity

To specifically explore the impact of the defective surface and $Ni(OH)_2$ decoration on HER activity, we have built several representative models of the local surface environments showing steps, one-layer cavities and $Ni(OH)_2$ decorated surface. Density functional theory (DFT) calculations was conducted on our models to probe the hydrogen (H) adsorption free energies on a series of adsorption sites. We have considered only the locally stable H structures to evaluate the HER activity using a previously established volcano type kinetic model between the H adsorption free energy and the HER rate[24].

We used 450 eV cut-off energy, MP smearing method with 0.2 eV smearing width for all the calculations. We used 5×5×1 K-points for systems with 4×4 or 5×5 unit cell, and 7×7×1 K-points for systems with 3×3 unit cell. We used 5 layers for all the models, and for the models with cavities, top three layers are fully relaxed, for the slab model and models with $Ni(OH)_2$ decoration, top two layers are fully relaxed, the convergence threshold is 0.01 eV/Å. All the DFT calculations are carried out by *VASP*.[i,ii]

Calculation of adsorption free energy

The adsorption free energy of H_2 is calculated by equation S1:

$$\Delta G_{nH} = G(\text{slab}+n\text{H}) - G(\text{slab}) - \frac{n}{2}G(\text{H}_2) \quad \text{(S1)}$$

G is the Gibbs free energy, and n is the number of adsorbed H atoms. We used the following equations to calculate the free energies:

$$G(\text{slab}+n\text{H}) = E(\text{slab}+n\text{H}) + ZPE(n^*\text{H}) + TS(n^*\text{H}) \quad \text{(S2)}$$

$$G(\text{slab}) = E(\text{slab}) \quad \text{(S3)}$$

$$\text{G}(\text{H}_2) = \text{E}(\text{H}_2) + ZPE(\text{H}_2) + TS(\text{H}_2) \quad \text{(S4)}$$

In equations S2, E(slab+nH) is the electronic energy of the metal slab with adsorbed H atoms, *H means the adsorbed H atom, ZPE (n*H) means the zero point energy of n adsorbed H atoms, T is the temperature, and S is the vibrational entropy. The latter two terms are calculated from the vibrational frequencies ν_i of the adsorbed H atoms by using equations S5-S6:

$$ZPE(n^*\mathrm{H}) = \sum_{i=1}^{3n} \frac{hv_i}{2} \tag{S5}$$

$$S(n^*\mathrm{H}) = \sum_{i=1}^{3n} \left\{ \frac{hv_i \exp(-hv_i / 2k_B T)}{k_B T[1-\exp(-hv_i / 2k_B T)]} - \ln\left[1-\exp(-hv_i / 2k_B T)\right] \right\} \tag{S6}$$

When calculating the vibrational frequencies of multiple adsorbed H atoms, we took off one bottom Pt layer to reduce the computational cost.

In equation S3, the free energy of the slab is approximated as the electronic energy of the slab.

In equation S4, we used $ZPE(H_2)$ = 0.27 eV and $TS(H_2)$ = 0.40 eV at T = 300K.

We express the adsorption free energy as $\Delta G_H - \Delta G_H^{Pt(111)}$ ($\Delta\Delta G$), which is the difference between the actual free energy ΔG_H and the adsorption free energy on Pt(111) surface $\Delta G_H^{Pt(111)}$. We used the Pt(111) surface model with 4×4 unit cell and 5 layers, and calculated that $\Delta G_H^{Pt(111)}$ = -0.290 eV.

Calculation of adsorption free energy in the solution with the effect of electron potential and pH.

$$\Delta G = G(\mathrm{slab}+n\mathrm{H}) - G(\mathrm{slab}) - \frac{n}{2} G(\mathrm{H_2}) - n\mu_{H^+ + e^-} \tag{S7}$$

$$\mu_{H^+ + e^-} = -eU_{SHE} - 2.3kTpH \tag{S8}$$

We used equation S7 to calculate the adsorption free energy with the impact of the reduction potential on the electrode, the first three terms on the right side are the same as the terms in equation

S1, the term $\mu_{H^+ + e^-}$ is the chemical potential of hydrogen ion and electron, which could be calculated using equation S8.[iii] U_{SHE} is the potential vs. standard hydrogen electrode

Furthermore, to determine which adsorption sites are accessible in the experimental conditions, we explored the occupied adsorption sites not only at low coverage condition, but also at high coverage condition, and compared the various coverage situations using first-principle atomistic thermodynamics.

The J-PtNWs present a variety of defect sites including atoms with lower and higher metallic coordination than the Pt (111) termination. Local surface environment at these sites have been described using three models: model A (Fig 3.10 A) and C (Fig 3.11) consist of a cavity on the Pt (111) surface while model B (Fig 3.12) is a Pt (553) stepped surface. All the potential adsorption sites for H have been explored on these surfaces. Several sites are not locally stable, in the sense that a small lateral displacement of the H atom would lead to a more stable adsorption situation. The HER activity for all locally stable sites is calculated using the volcano-type kinetic model, which expresses the exchange current i_0 as a function of H adsorption free energy (Fig 3.10 B).[24] The activity optimum appears for a site with H-binding energy 0.09 eV weaker than that on the hollow sites occupied on Pt (111).[24] It is obvious that many sites show binding energy near the optimum value.

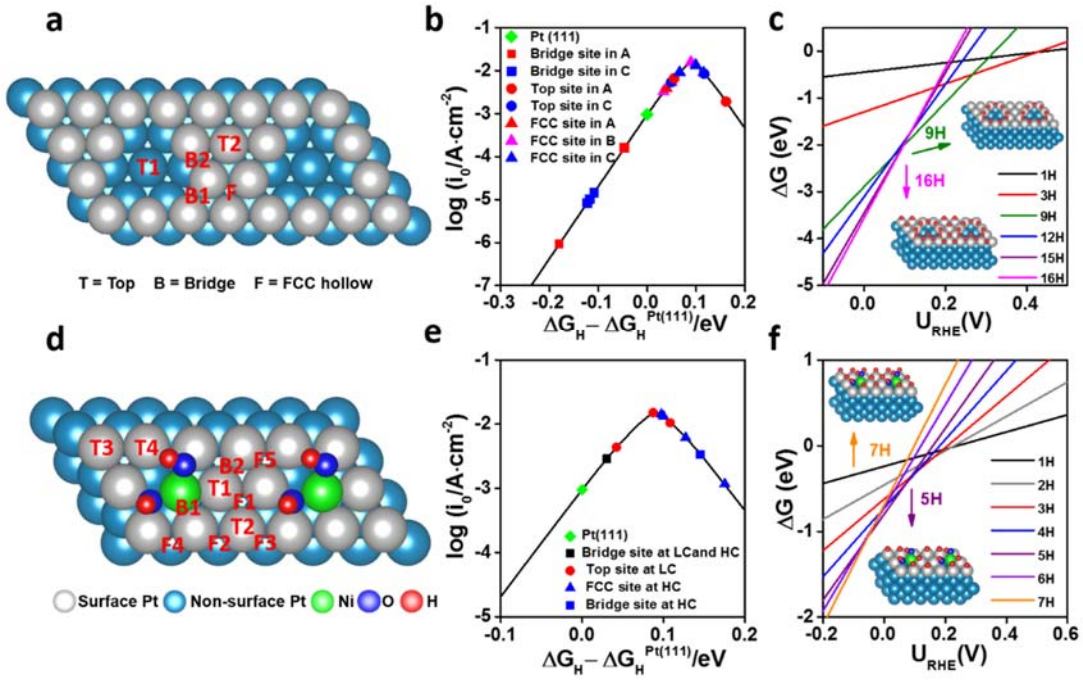

Figure 3.10. (**A**) Cavity defect on Pt (111) surface (Model A). The unit cell is 4×4, and the figure shows 2 unit cells. The locally stable adsorption sites for the H atom are labeled on the top view model. (**B**) Exchange current i_0 for HER as a function of *H adsorption free energy for the locally stable adsorption sites in Models A, B and C (The structures of Model B and C are in supporting information). (**C**) Adsorption free energy of hydrogen on model A Pt surface as a function of the applied potential U_{RHE} at various coverage in pH=14 solution. (**D**) Model D for $Ni(OH)_2$ decorated Pt(111) surface (Ni is substituting a Pt surface atom). The unit cell is 3×3, and the figure shows two unit cells. (**E**) Volcano curve for adsorption sites on model D at low coverage (LC) and high coverage (HC) conditions. (**F**) Adsorption free energy of hydrogen on model D as a function of U_{RHE} at various coverage in pH=14 solution.

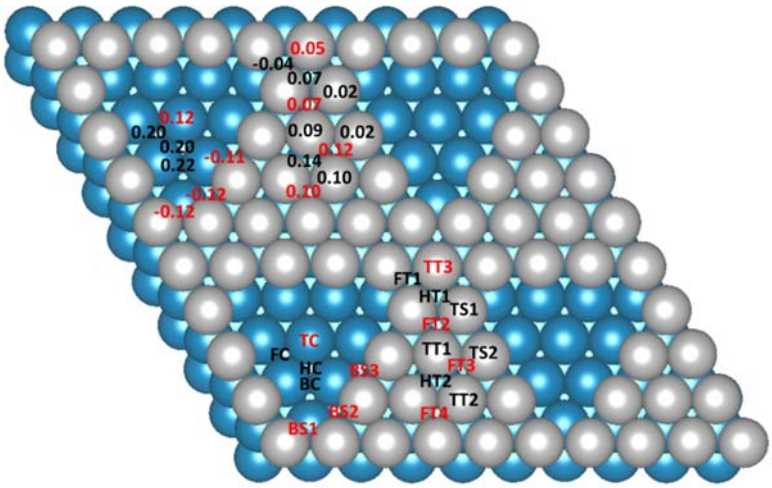

Figure 3.11. Model C with 5×5 unit cell and 5 layers. Model C has a larger cavity than Model A, but there are many similarities. The BS sites are still the most stable sites. The TS sites have lower energies than TT3, FT2 and FT3, but they are blocked by the BS sites, so the local minima sites on the terrace are TT3, FT2, FT3 and FT4. The TC site in the cavity is still a local minimum site.

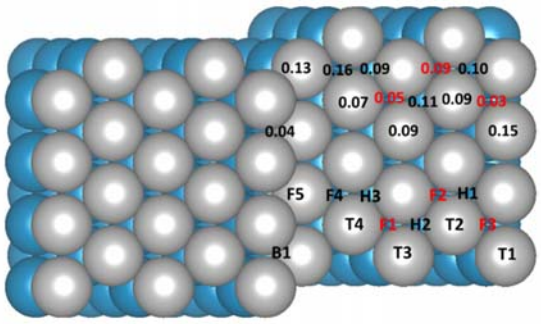

Figure 3.12. Model B of Pt(553) stepped surface.

The defective models show a large distribution of binding strengths. Bridge sites on the ridge of the cavities are clearly more stable than hollow sites on Pt(111), but accordingly poorly active for HER. The *fcc* sites on the defective surface models are less stable than those on Pt (111) by

0.03 to 0.1 eV. This destabilization makes these sites more active and is induced by compressive strain on the defective surface compared to Pt (111) (Fig 3.13). Top sites are not stable on Pt(111) (they diffuse to *fcc* hollow sites), but interestingly they become locally stable both inside the cavity and on the upper terrace close to the ridge on the defective models (see T1 and T2 on model A for example). These top sites show a weaker H-binding energy versus hollow sites on Pt (111) and are placed in the highly active zone.

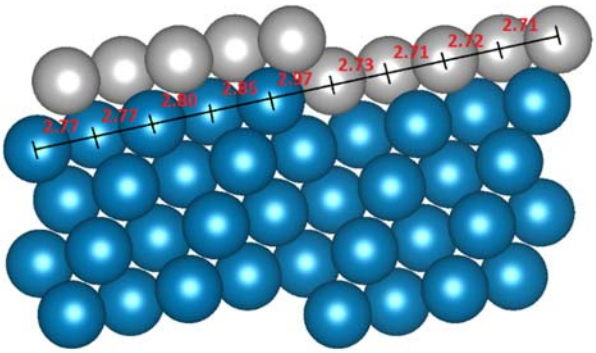

Figure 3.13. Bond lengths (Å) in model B. The Pt-Pt distance in bulk is 2.81 Å. Model B is Pt(553) surface and it's a model for the step defect. We find the fcc hollow sites, such as F1, F2 and F3 are destabilized compared to Pt(111), which could be explained by the strain effect. In figure 11, we can see that the bond lengths between the terrace atoms are about 3.5% less than the normal distance in the Pt bulk.

When considering all sites together, the hydrogen atoms will first occupy the inactive bridge sites at low coverage, and then occupy the active top and *fcc* hollow site with increasing coverage. It is hence crucial to determine the H coverage in realistic conditions. The total adsorption free energy at different H coverage is shown in Fig. 3c as a function of the electrode potential (referenced to the reversible hydrogen electrode; U_{RHE}). For model A, in pH=14 solution, a low

coverage (1/16 ML) is favored for a U_{RHE} > 0.4 V, while below 0.25 V the H coverage strongly rises to 9/16 ML (occupation of 3 B1 sites and 6 B2 sites in Fig 3.10 A). For a potential below 0.1 V, sites that are more active than Pt (111) begin to be populated (3 F sites, then 3 T2 sites and 1 T1 site). At the experimental potential of 0.07 V (-70 mV vs. RHE), a high coverage of 1ML is reached, with occupation of both active (7/16 ML) and inactive (9/16 ML) sites. The significant density of highly active sites contributes to the extraordinary activity observed in the J-PtNWs. The influence of Ni at the surface of the Pt catalyst is modeled by single Ni atoms inserted in the first layer of a Pt(111) surface. In the considered basic conditions, two OH groups bind to surface Ni atom (Fig. 3.10 D). Fig. 3.10 E shows the HER activity predicted from the volcano curve for the stable adsorption sites at low and high H coverage conditions, because the adsorption sites are different at different coverage. In model D, H adsorbs preferentially on Pt-Ni bridge site and then on the top Pt sites (T1-T3, then T4 will be occupied because all other sites are blocked by either hydroxyl groups or other top sites with H). However at high coverage, occupation of slightly less stable hollow sites F1-F4 together with bridge B1 and B2 becomes favored over top site occupations because a larger number of favorable sites can be obtained (Fig 3.14). All the sites on this $Ni(OH)_2$ decorated Pt surface are more active than those on Pt (111) at either low or high coverage. At experimental condition (U_{RHE} = -0.07 V), 5 H atoms adsorb per unit cell, although configurations with 4 to 7 H are close in energy (Fig. 3.10 F), and all the 5 adsorption sites are more active than Pt (111) surface sites. **The $Ni(OH)_2$ decoration will only create active sites, while the defective Pt (111) models creates both inactive and active sites, explaining why $Ni(OH)_2$ decorated J-PtNWs have even higher HER activities than J-PtNWs.**

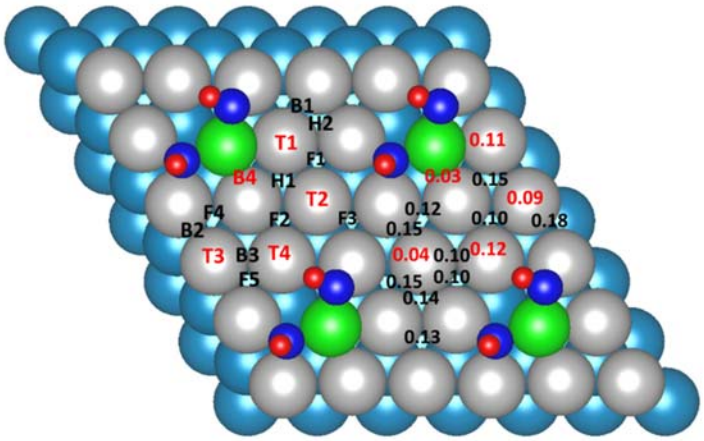

Figure 3.14. Model D with 3×3 unit cell and 5 layers. Model D is the $Ni(OH)_2$ decorated Pt(111) surface. B1 is the most preferred site, then T3, T2 and T1 sites will be covered if more H is adsorbed. Since all the other sites are blocked, T4 will be covered if one more H atom comes in although it's not a local minimum. If higher coverage is reached, the fcc sites and B2 site rather than the top sites will be covered.

3.5 Conclusion

In summary, we have designed an electrochemical dealloying - decoration synergetic method to modify the surface of ultrafine jagged platinum nanowire with nickel hydroxide species. By combining XPS, EXAFS analyses with STEM study, we verify that the defective 1-D nanostructure was successfully coated with $Ni(OH)_2$. Electrochemical catalytic test revealed that the resulting J-PtNWs and J-PtNWs/$Ni(OH)_2$ both have exceptional HER activity. Additionally, after our electrochemical processes, such defective platinum surface feature and $Ni(OH)_2$ decoration will also change the originally OER-nerdy platinum into an OER active material, and make the platinum-based nanowires become a mass-effective bifunctional electrolyzer. As

demonstrated by both theoretical calculations and experiment studies, the defective nature of the surface generated from electrochemical de-alloying creates an ensemble of sites, a majority of them lowering the H adsorption free energies towards optimal value, hence increasing the density of highly active sites. DFT study also reveals that $Ni(OH)_2$ decoration overall destabilizes H binding energy and hence only creates more active sites on jagged Pt suface, thus enabling the record HER activity of J-PtNWs/$Ni(OH)_2$.

3.6 References

1. M. Dresselhaus, I. Thomas, Alternative energy technologies. *Nature* **414**, 332 (2001).

2. P. C. Vesborg, B. Seger, I. Chorkendorff, Recent development in hydrogen evolution reaction catalysts and their practical implementation. *The journal of physical chemistry letters* **6**, 951 (2015).

3. J. A. Turner, Sustainable hydrogen production. *Science* **305**, 972 (2004).

4. M. Jacobson, W. Colella, D. Golden, Cleaning the air and improving health with hydrogen fuel-cell vehicles. *Science* **308**, 1901 (2005).

5. L. M. Gandía, R. Oroz, A. Ursúa, P. Sanchis, P. M. Diéguez, Renewable hydrogen production: performance of an alkaline water electrolyzer working under emulated wind conditions. *Energy & Fuels* **21**, 1699 (2007).

6. D. Kong, H. Wang, Z. Lu, Y. Cui, CoSe2 nanoparticles grown on carbon fiber paper: an efficient and stable electrocatalyst for hydrogen evolution reaction. *Journal of the American Chemical Society* **136**, 4897 (2014).

7. Y. Zheng *et al.*, Toward design of synergistically active carbon-based catalysts for electrocatalytic hydrogen evolution. *ACS nano* **8**, 5290 (2014).

8. N. M. Markovića, S. T. Sarraf, H. A. Gasteiger, P. N. Ross, Hydrogen electrochemistry on platinum low-index single-crystal surfaces in alkaline solution. *Journal of the Chemical Society, Faraday Transactions* **92**, 3719 (1996).

9. R. Subbaraman *et al.*, Origin of anomalous activities for electrocatalysts in alkaline electrolytes. *The Journal of Physical Chemistry C* **116**, 22231 (2012).

10. Z. Cao *et al.*, Platinum-nickel alloy excavated nano-multipods with hexagonal close-packed structure and superior activity towards hydrogen evolution reaction. *Nature Communications* **8**, (2017).

11. W. Sheng, H. A. Gasteiger, Y. Shao-Horn, Hydrogen oxidation and evolution reaction kinetics on platinum: acid vs alkaline electrolytes. *Journal of The Electrochemical Society* **157**, B1529 (2010).

12. P. Rheinländer, S. Henning, J. Herranz, H. A. Gasteiger, Comparing hydrogen oxidation and evolution reaction kinetics on polycrystalline platinum in 0.1 M and 1 M KOH. *ECS Transactions* **50**, 2163 (2013).

13. W. Sheng, M. Myint, J. G. Chen, Y. Yan, Correlating the hydrogen evolution reaction activity in alkaline electrolytes with the hydrogen binding energy on monometallic surfaces. *Energy & Environmental Science* **6**, 1509 (2013).

14. R. Subbaraman *et al.*, Enhancing hydrogen evolution activity in water splitting by tailoring Li+-Ni (OH) 2-Pt interfaces. *Science* **334**, 1256 (2011).

15. N. Danilovic *et al.*, Enhancing the alkaline hydrogen evolution reaction activity through the bifunctionality of Ni (OH) 2/metal catalysts. *Angewandte Chemie* **124**, 12663 (2012).

16. M. Li *et al.*, Ultrafine jagged platinum nanowires enable ultrahigh mass activity for the oxygen reduction reaction. *Science* **354**, 1414 (2016).

17. H. Yin *et al.*, Ultrathin platinum nanowires grown on single-layered nickel hydroxide with high hydrogen evolution activity. *Nature communications* **6**, (2015).

18. F. W. Lytle, Determination of d-band occupancy in pure metals and supported catalysts by measurement of the LIII X-ray absorption threshold. *Journal of Catalysis* **43**, 376 (1976).

19. D. Pearson, C. Ahn, B. Fultz, White lines and d-electron occupancies for the 3d and 4d transition metals. *Physical Review B* **47**, 8471 (1993).

20. N. Becknell *et al.*, Atomic structure of Pt3Ni nanoframe electrocatalysts by in situ X-ray absorption spectroscopy. *J. Am. Chem. Soc* **137**, 15817 (2015).

21. Y. Zhu *et al.*, Ultrathin nickel hydroxide and oxide nanosheets: synthesis, characterizations and excellent supercapacitor performances. *Scientific reports* **4**, 5787 (2014).

22. J. Nai *et al.*, Efficient electrocatalytic water oxidation by using amorphous Ni–Co double hydroxides nanocages. *Advanced Energy Materials* **5**, (2015).

23. P. Wang *et al.*, Precise tuning in platinum-nickel/nickel sulfide interface nanowires for synergistic hydrogen evolution catalysis. *Nature Communications* **8**, (2017).

24. J. K. Nørskov *et al.*, Trends in the exchange current for hydrogen evolution. *Journal of The Electrochemical Society* **152**, J23 (2005).

25. G. Kresse, J. Hafner, Ab initio molecular dynamics for liquid metals. *Physical Review B* **47**, 558 (1993).

26. G. Kresse, J. Hafner, Ab initio molecular-dynamics simulation of the liquid-metal–amorphous-semiconductor transition in germanium. *Physical Review B* **49**, 14251 (1994).

27. J. P. Perdew, K. Burke, M. Ernzerhof, Generalized gradient approximation made simple. *Physical review letters* **77**, 3865 (1996).

28. P. E. Blöchl, Projector augmented-wave method. *Physical review B* **50**, 17953 (1994).

Chapter 4. Conclusion

In conclusion, by engineering the overall morphology and surface configuration of platinum-based nanomaterial, we are able to greatly enhance the area specific activity and electro-chemically active surface area (ECSA) simultaneously for electro-catalytic reactions such as oxygen reduction reaction and alkaline water electro-catalysis.

In our first work, our de-alloying strategy could change the composition of originally Ni-rich Pt-Ni nanowire to pure platinum while still maintain its one-dimensional structure. The jagged platinum nanowire features an ultrafine diameter as small as 2nm, which result in a high ECSA of 118 $m2/g_{Pt}$ and 1.6 times higher than that of state-of-art commercial Pt/C materials. Electro-chemical performance tests reveal that such J-PtNWs exhibits 52 times higher ORR mass activity when compare with our bench mark Pt/C, which present a huge leap for platinum utilization efficiency. Moreover, STEM and EXAFS study demonstrate that the nickel leaching creates numerous defectives sites on nanowire surface, and the strain of J-PtNWs was tuned by 1.8% compare with bulky platinum. Additional simulation results help confirm that this jagged geometry are stressed, under-coordinated, and crystalline-like. Also it has unusually high number of surface rhombi, which could significantly accelerate the sluggish ORR kinetics.

In our second work, we used a controllable de-alloying method combine with an electro-chemical decoration process to grow a stabilized nickel hydroxide species on defective platinum nanowire surface. XPS and EXAFS studies shows the Ni chemical state and coordination environment is consistent with $Ni(OH)_2$. The result J-PtNWs/$Ni(OH)_2$ hybrid material exhibit an record high HER mass activity of 11.8A/mgPt at -0.07V *vs.* RHE (pH14), which is 17 times higher than Pt/C bench mark. Density functional theory calculations reveal that the defective sites will tune the H-binding energy towards the optimum value, and the $Ni(OH)_2$ decoration will only create

active sites on defective Pt model. Furthermore, out oxygen evolution reaction tests shows a much improved OER activity for J-PtNWs after the addition of $Ni(OH)_2$, which indicates that the J-PtNWs/$Ni(OH)_2$ could be a superior bifunctional material for alkaline water electro-catalysis.